Chapter 5

Role of ferroelectric soft phonon mode (Γ_4^-) in tuning the inter-ferroelectric phase boundary of lead-free $(Ba_{0.92}Ca_{0.08})(Zr_{0.05}Ti_{0.95-x}Sn_x)O_3$; $(0 \leq x \leq 0.10)$ system for enhanced ferroelectric polarization

5.1 Introduction

Perovskites (ABO_3)-based compounds host a wide variety of physical phenomena, such as ferroelectricity, ferromagnetism, and ferroelasticity, that can be effectively tuned via a slight distortion in the crystallographic structure [68, 92]. The structural distortions in perovskites can be expressed in terms of various irreducible representations (irreps)

corresponding to the high-symmetry parent structure [93]. For example, the structures exhibiting octahedral rotation(s) can be effectively tuned by manipulating 'A' site ionic radii [76]. If the adjacent octahedra rotate in the same direction, then the tilting will be associated with the zone boundary irrep (M_3^+) corresponding to [$k = (\frac{1}{2},\frac{1}{2},0)$] point of the cubic Brillouin zone, whereas if the adjacent octahedra rotate in opposite direction, then the tilting will be associated with the zone boundary irrep (R_4^+) corresponding to [$k = (\frac{1}{2},\frac{1}{2},\frac{1}{2})$] point of the cubic Brillouin zone [69, 92, 93]. In addition, another feature termed as 'octahedral distortions' results due to either change in B-O bond length or deviation of O-B-O angle from 90^o or 180^o. Some of the irreps which lead to octahedral distortions are X_5^+, M_2^+, R_5^+ etc., corresponding to [$k = (0,\frac{1}{2},0)$], [$k = (\frac{1}{2},\frac{1}{2},0)$], and [$k = (\frac{1}{2},\frac{1}{2},\frac{1}{2})$] point of the cubic Brillouin zone, respectively [94]. Further, the structural distortions associated with the off-centering of the 'B' site cation is driven by the instability associated with the Γ[$k = (0,0,0)$] point of the cubic Brillouin zone [69, 93]. The structural phase transitions driven by the condensation of the phonon mode corresponding to the zone center are termed as ferrodistortive [21]. However, if the associated phonon mode is polar in nature (associated irrep Γ_4^-), then its condensation leads to a long-range polar ordering in the material termed as 'ferroelectricity' [69]. Although most of the ferroelectric phase transitions are ferrodistortive, but sometimes, it may not be so. Whenever a coupling between the modes exists, it is not necessary that the zone center polar mode instability is driving the phase transition to a ferroelectric phase. Sometimes, a driving antidistortive mode (a mode corresponding to other than zone center) couples to a mode belonging to zone center, and its condensation induces a small polarization in the material in an indirect fashion. In such a case, the antidistortive mode act as a 'primary order parameter' while the spontaneous polarization becomes the 'secondary order parameter' [21]. Thus it becomes interesting to correlate the physical response of any ferroelectric ceramic system with the

amplitudes of the frozen phonon modes (irreps), which drive the structural phase transition with respect to a parent high symmetry phase.

In this chapter, we have fabricated a B(Sn^{4+}) site-modified eco-friendly barium titanate ($BaTiO_3$)-based solid solution $(Ba_{0.92}Ca_{0.08})(Zr_{0.05}Ti_{0.95\text{-}x}Sn_x)O_3$; BCZTSn$x$ $(0 \leq x \leq 0.10)$, where Sn(x) doping has induced an inter-ferroelectric three-phase coexistence at room temperature, with significantly enhanced amplitudes of ferroelectric Γ_4^- phonon mode than the host composition leading to significantly improved physical properties, which makes the ceramics a suitable candidate for various application purposes.

5.2 Experimental Procedure

The $(Ba_{0.92}Ca_{0.08})(Zr_{0.05}Ti_{0.95\text{-}x}Sn_x)O_3$; BCZTSn$x$ $(0 \leq x \leq 0.10)$ ceramics have been synthesized via a conventional solid-state reaction route. The stoichiometric fractions of the raw materials $BaCO_3$, $CaCO_3$, ZrO_2, SnO_2, and TiO_2 were mixed, and ball milled for 24 hours in ethanol media. The obtained powder mixtures were dried and thereafter calcined at 1100 ^{0}C for 6 hours. After calcination, the powders were again crushed and mixed with polyvinyl alcohol (PVA) binder. Thereafter it was pelletized in the form of discs of diameter $\sim$ 10 mm and thickness $\sim$ 1.3 mm, and then these pellets were sintered at 1350 ^{0}C for 12 hours. Thereafter the density of the sintered pellets was measured using the Archimedes method. A relative density of more than 97% was found to be exhibited by the sintered pellets of all the compositions.

To analyse the crystallographic phase and purity of the synthesized ceramics, the powder X-ray diffraction measurements were performed on a 9 kW rotating anode based Rigaku SmartLab high-resolution X-ray diffractometer operated in Bragg–Brentano geometry. To perform the X-ray diffraction measurements, the sintered pellets were crushed in the form of fine powders, and then the powders were annealed at 300 ^{0}C for 4 hours to remove any induced strain if occurred during crushing. The X-ray diffraction data have

been collected over the 2θ range 20^0 to 120^0 with a step size of 0.02, by using Cu-$K_{\alpha 1}$ (1.54059 Å) radiation. The data were recorded in a continuous scan mode. The analysis of the data shows the solid solution formation for the whole analysed composition range, *i.e.,* $0 \leq x \leq 0.10$, except a minor impurity phase of $Ba_4Ti_{13}O_{30}$, having a fraction <1%. To fix the crystallographic structure of the synthesized ceramics, we performed the Rietveld refinements of the X-ray diffraction pattern using the FULLPROF software [213]. During refinement, the peak profile was modeled using the pseudo-Voigt function. The background was modeled using linear interpolation between a set background points with refinable heights. To get the best fit between observed and simulated patterns, the parameters like lattice parameter, profile parameter, scale factor, zero displacement, thermal parameters, and positional coordinates were refined. For dielectric measurements, both the top and bottom surfaces of the sintered pellets were polished and cleaned gently. Thereafter, these pellets were electroded with fired-on silver paste, which was first dried at 100 ^{0}C and thereafter cured at 600 ^{0}C for 10 min, and temperature-dependent dielectric measurements were performed using a Keysight E4990A impedance analyzer with the heating rate 2 ^{0}C/min. The microstructural observations were performed using a high-resolution scanning electron microscope (HR-SEM: Nova Nano SEM 450, FEI Company of USA (S.E.A.) PTE, LTD) to observe the variation in grain size and its correlation with measured physical properties as a function of Sn(x) content. The average grain size has been calculated by performing the Lorentz fit of the histogram plot of the grain size measured via image J-software. In addition, to have a better insight into the composition-dependent phase transitions, the room temperature Raman spectroscopic measurements has been carried out for all the compositions by using the Renishaw InVia Raman spectrometer (Wotton-under-Edge, UK) using 532 nm diode-pumped solid-state laser. The resolution of the Raman spectrometer is $\sim$ 1 cm^{-1}. To characterize the ferroelectric nature of various compositions, the room temperature polarization *vs.* electric field, *i.e.,* PE hysteresis loops measurements, were

performed using Radiant Technology's Precision Material Analyzer Workstation based on the virtual ground system at 50 Hz frequency. The results interpretations have been assisted by symmetry mode analysis, performed using the 'AMPLIMODES' [265, 266] program available at Bilbao crystallographic server. Further, to see the effect of Sn(x) on various phase transitions, temperature-dependent Raman spectroscopic studies were carried out. The temperature-dependent Raman measurement was carried out using Horiba LabRAM HR at an excitation wavelength of 514.5 nm via Argon ion gas laser.

5.3 Results and discussions

5.3.1 Microstructural analysis

The microstructural features of all the ceramics are shown in Fig. 5.1. The analysis reveals that all the BCZTSnx ceramics show well-developed grains; however, some intergranular pores were observed. Further, the average grain size has shown a decreasing trend from x = 0 ($\sim$ 23 μm) to $x = 0.10$ ($\sim$ 17 μm), as shown in Fig. 5.2. The decrease in the grain size of BCZTSnx ceramics as a function of Sn(x) may be due to the slow diffusion of Sn^{4+} (69 pm) cations having larger mass and ionic radii than Ti^{4+} (61 pm) cations as depicted in previous studies [163, 267].

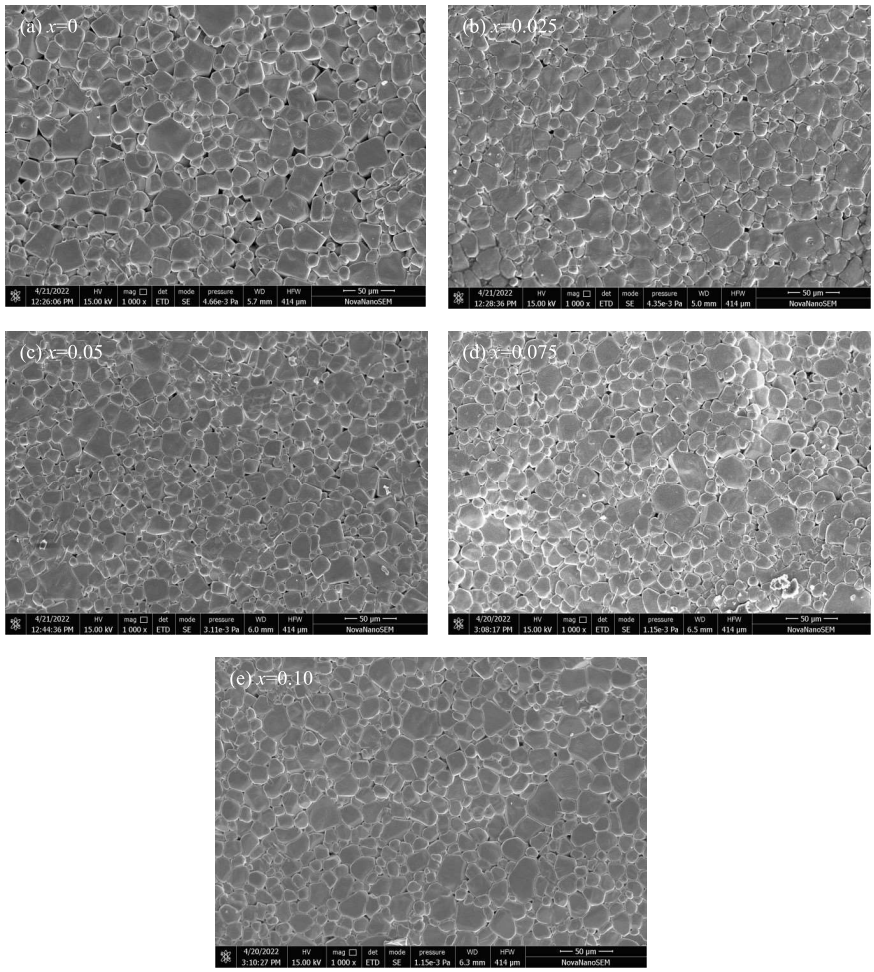

Fig. 5.1 High-resolution scanning electron micrographs of the sintered pellets of BCZTSnx $(0 \leq x \leq 0.10)$ ceramics.

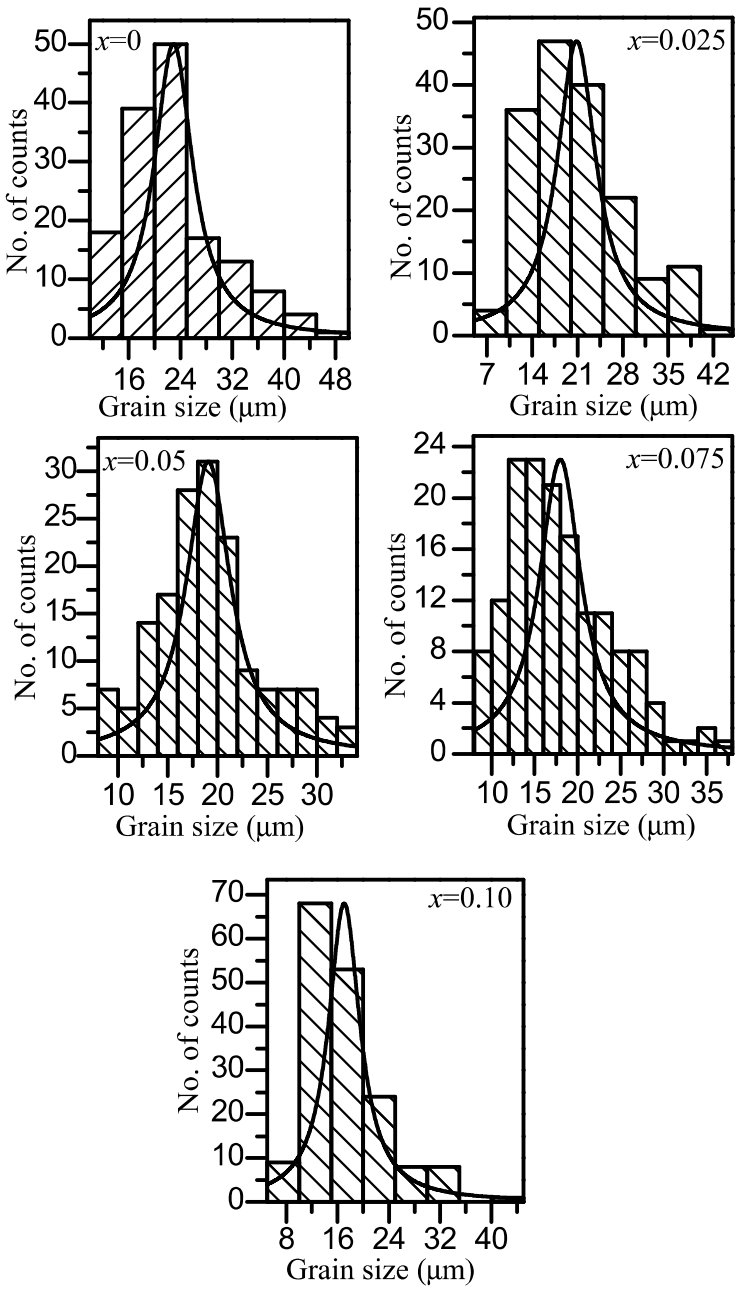

Fig. 5.2 The histograms depicting the grain size distribution in BCZTSnx $(0 \leq x \leq 0.10)$ ceramics.

5.3.2 Dielectric studies

Fig. 5.3 shows the temperature-dependent variation of dielectric permittivity for all the synthesized ceramic compositions, *i.e.,* $(0 \leq x \leq 0.10)$. Both the real ($\varepsilon^{'}$) and imaginary ($\varepsilon^{''}$) of dielectric permittivity *vs.* temperature curve shows a decrease in paraelectric to ferroelectric phase transition temperature, while an increase in inter-ferroelectric phase transition temperatures, *viz.,* tetragonal-orthorhombic (T-O), and orthorhombic-rhombohedral (O-R), as a function of Sn(x) content. For x = 0, we observed a single anomaly corresponding to the paraelectric (cubic) to ferroelectric (tetragonal) phase transition. For the same composition, the temperature-dependent phase diagram proposed by Singh *et al.* has demonstrated the appearance of all phases corresponding to pure $BaTiO_3$ [268, 269], which indicates that the other two-phase transitions, *viz.,* T-O and O-R, for x = 0, lie below the room temperature (30 ^{0}C). Thus the dielectric study suggests a single tetragonal phase for x = 0 at room temperature. For x = 0.025, another anomaly appears in the vicinity of room temperature, in addition to the anomaly corresponding to the cubic to tetragonal phase transition as observed for x = 0. This anomaly for x=0.025 corresponds to the ferroelectric tetragonal (T) to orthorhombic (O) phase transition. On further increasing the Sn(x) content, *i.e.,* x = 0.05, the O-T phase transition corresponding to x = 0.025 shows a shift toward higher temperatures. Further, for x = 0.075, all the three-phase transitions are merged, and the paraelectric to ferroelectric phase transition temperature is lying slightly above room temperature, leading to a ferroelectric rhombohedral phase at ambient conditions. Thus the dielectric study suggests that the effect of Sn(x) doping on the phase transition behaviour of BCZTSnx is similar to the one reported for $Ba(Sn_xTi_{1-x})O_3$ and $Ba(Zr_xTi_{1-x})O_3$ ceramics [8, 180]. On further increasing Sn(x) content, the paraelectric (cubic) to ferroelectric (rhombohedral) phase transition has again shown a shift towards low temperatures, leading to the stabilization of a (cubic+rhombohedral) phase coexistence at the room temperature for x = 0.10. Owing to the appearance of paraelectric to ferroelectric

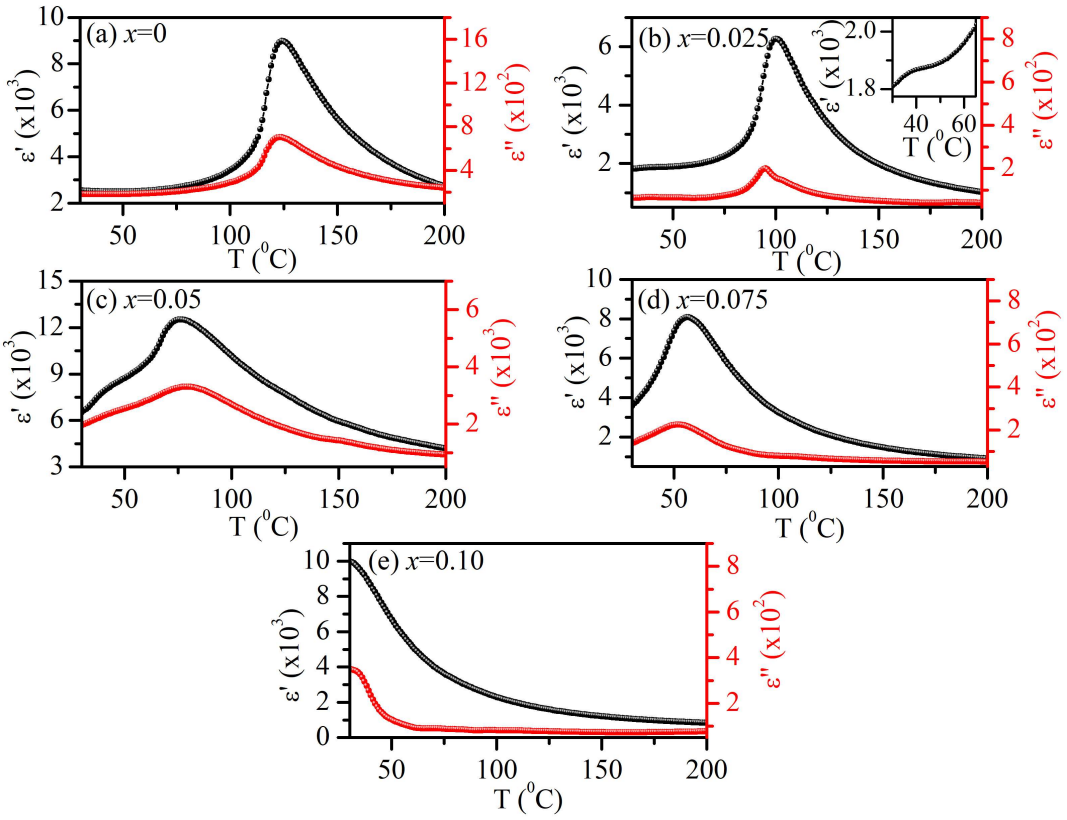

Fig. 5.3 Variation in real ($\varepsilon^{'}$) and imaginary ($\varepsilon^{''}$) parts of dielectric permittivity as a function of temperature for BCZTSnx ($0 \leq x \leq 0.10$) ceramics at 143 kHz.

phase transition at room temperature, the dielectric permittivity has shown a many-fold increment for $x = 0.10$ ($\varepsilon' = 9987$) than the host composition $x = 0$ ($\varepsilon' = 2539$).

5.3.3 Raman spectroscopic analysis

The room temperature Raman spectra of the BCZTSnx ($0 \leq x \leq 0.10$) ceramics, measured over the wavenumber range 50-1000 cm^{-1}, is shown in Fig. 5.4. To analyse the Raman spectra of $BaTiO_3$-based ceramics, the temperature-dependent Raman spectra of barium titanate was used for the interpretation of various phase transitions. The perovskite $BaTiO_3$ ceramic consists of five atoms per unit cell, which gives rise to 12 optical modes of vibrations. The optical phonon modes corresponding to the Γ point, in the cubic phase

Table 5.1 Factor group analysis of phonons in $BaTiO_3$.

Space group: $Pm\bar{3}m$			Space group: $P4mm$		
Atoms	WP	Irrep's	Atoms	WP	Irrep's
Ba	1a	T_{1u}	Ba	1a	A_1+E
Ti	1b	T_{1u}	Ti	1b	A_1+E
O	3c	$2T_{1u}$+T_{2u}	O_1	1b	A_1+E
			O_2	2c	(A_1+E)+(E+B_1)
Γ_{total}		$4T_{1u}$+T_{2u}			$4A_1$+5E+B_1
$\Gamma_{acoustic}$		T_{1u}			A_1+E
$\Gamma_{optical}$		$3T_{1u}$+T_{2u}			$4A_1$(R)+5E(R)+B_1(R)
Space group: $Pm\bar{3}m$			Space group: $Amm2$		
Atoms	WP	Irrep's	Atoms	WP	Irrep's
Ba	1a	T_{1u}	Ba	2a	A_1+B_1+B_2
Ti	1b	T_{1u}	Ti	2b	A_1+B_1+B_2
O	3c	$2T_{1u}$+T_{2u}	O_1	2a	A_1+B_1+B_2
			O_2	4e	(A_1+B_1+B_2)+(A_1+A_2+B_2)
Γ_{total}		$4T_{1u}$+T_{2u}			$5A_1$+A_2+$4B_1$+$5B_2$
$\Gamma_{acoustic}$		T_{1u}			A_1+B_1+B_2
$\Gamma_{optical}$		$3T_{1u}$+T_{2u}			$4A_1$(R)+A_2(R)+$3B_1$(R)+$4B_2$(R)
Space group: $Pm\bar{3}m$			Space group: $R3m$		
Atoms	WP	Irrep's	Atoms	WP	Irrep's
Ba	1a	T_{1u}	Ba	3a	A_1+E
Ti	1b	T_{1u}	Ti	3a	A_1+E
O	3c	$2T_{1u}$+T_{2u}	O	9b	2(A_1+E)+(A_2+E)
Γ_{total}		$4T_{1u}$+T_{2u}			$4A_1$+A_2+5E
$\Gamma_{acoustic}$		T_{1u}			A_1+E
$\Gamma_{optical}$		$3T_{1u}$+T_{2u}			$3A_1$(R)+A_2+4E(R)

$\Gamma_{optical}$; 'R' corresponds to Raman active modes.

having $Pm\bar{3}m$ space group, belong to $3T_{1u}$+T_{2u} irreducible representations [239, 261]. Both T_{1u} and T_{2u} modes exhibit a triply degenerate nature and possess an odd symmetry with respect to the inversion center, and hence are Raman inactive in nature [238]. When the cubic phase of $BaTiO_3$ transforms into a tetragonal phase, the T_{1u} mode gives rise to A_1 and E modes while the T_{2u} mode transforms into the B_1 and E modes (see Table 5.1) [238, 239]. For the orthorhombic phase, the optical vibrations belonging to the T_{1u} mode of the cubic phase split into A_1, B_1, and B_2 modes, while those corresponding to the T_{2u} modes split into A_1, A_2, and B_2 modes, with all of them being Raman active

[238, 270]. Further, the modes corresponding to the T_{1u} phonons split into A_1 and E modes, while those corresponding to the T_{2u} phonons get split into A_2, and E modes for the low-temperature rhombohedral phase of $BaTiO_3$ [239, 257]. Out of these, A_1 and E modes exhibit Raman active nature, and A_2 mode is Raman inactive [239, 257]. The

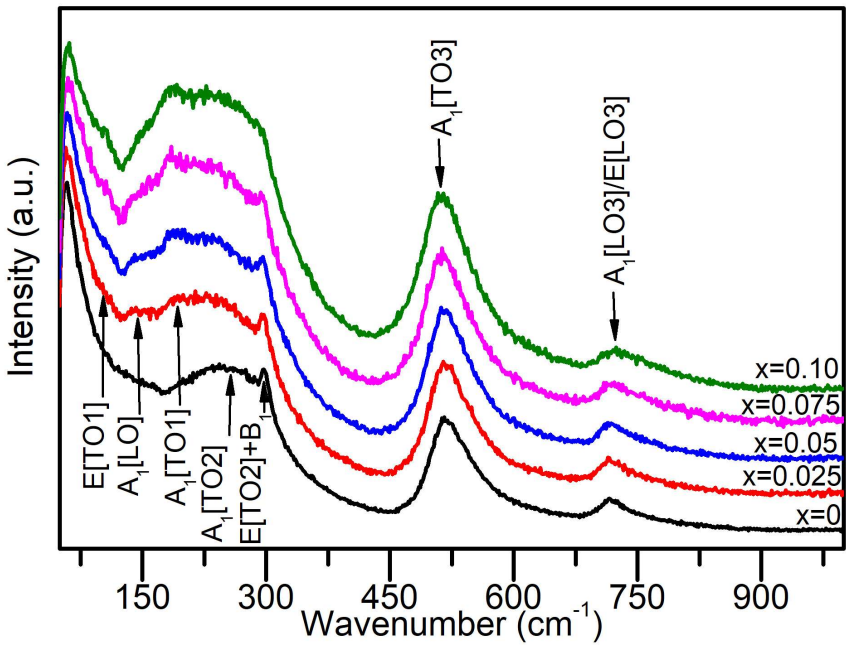

Fig. 5.4 Raman spectra of BCZTSnx ($0 \leq x \leq 0.10$) ceramics measured at room temperature.

measured Raman spectra for all the compositions exhibit different modes, *viz.,* E[TO1] around 106 cm^{-1}, A_1[LO] around 150 cm^{-1}, A_1[TO1] around 193 cm^{-1}, A_1[TO2] around 265 cm^{-1}, E[TO2]+B_1 around 300 cm^{-1}, A_1[TO3] around 520 cm^{-1} and A_1[LO3]/E[LO3] around 719 cm^{-1}. In addition to these modes, the appearance and disappearance of the two dips have been observed around 125 and 176 cm^{-1} as a function of Sn(x) content. The dip present around 125 cm^{-1} appears due to different 'B' cations in the perovskite (ABO_3) structure, and its intensity is related to the increased concentration of the substituted cation corresponding to the 'B' site [189, 264]. For x = 0, it seems to be very shallow, and with an increase in Sn(x) content, it becomes more and more pronounced (see Fig. 5.4).

Further, the dip around 176 cm^{-1} has been considered to be caused by the interference effect of A_1[TO1] and A_1[TO2] phonon modes [189, 264]. The above-mentioned A_1[TO1] mode corresponds to the displacement of the 'B' site and oxygen ions with respect to the 'A' site cation, and it is related to the ferroelectric nature of the materials [239]. The A_1[TO2] mode also belongs to the ferroelectricity and corresponds to the displacement of the 'B' site cations with respect to both the 'A' site and oxygen ions [239]. In $BaTiO_3$, the existence of the sharp E[TO2]+B_1 mode around 300 cm^{-1} and the A_1[LO3]/E[LO3] mode around 719 cm^{-1}, along with a dip present around 176 cm^{-1}, has been considered as the signature of the tetragonal phase [164, 184]. The presence of all these peaks for $x = 0$ and a broad peak around 265 cm^{-1} corresponding to the A_1[TO2] mode clearly suggests a tetragonal structure for this composition [164, 184, 227], in agreement with the structure concluded from dielectric studies. On further increasing the Sn(x) content, some significant changes appear in the band centered around 100-300 cm^{-1}. The previous studies have revealed that the new A_1[TO1] mode occurs in orthorhombic or rhombohedral phases in contrast to cubic or tetragonal phases [227]. The A_1[TO1] mode has been considered as a characteristic of the orthorhombic phase [227]. The appearance of this peak can be clearly seen in the Raman spectra of $x = 0.025$. Also, the measured Raman spectra of $x = 0.025$ exhibit the presence of the characteristic peak of the rhombohedral phase corresponding to A_1[LO] mode around 150 cm^{-1} and E[TO1] mode around 106 cm^{-1}, which occurs only in the rhombohedral phase [264]. However, the dielectric studies for $x = 0.025$ show a tetragonal and orthorhombic phase transition in the vicinity of room temperature. Thus, based on combined dielectric and Raman spectroscopic studies, a three-phase (tetragonal+orthorhombic+rhombohedral) coexistence has been concluded for $x = 0.025$. Recently, a similar three-phase coexistence has been reported by Zhu *et al.* in (Ba,Ca)(Sn,Ti)O_3 system, using combined dielectric and Raman spectroscopic studies [204]. For $x = 0.05$, the peaks are similar to $x = 0.025$, whereas the peak around 106 cm^{-1}

become more prominent, indicating the strengthening of the rhombohedral phase. Further, the dielectric studies have shown that the orthorhombic to rhombohedral phase transition for $x = 0.05$ lies in the vicinity of room temperature. Thus, the combined dielectric and Raman spectroscopic study show an orthorhombic and rhombohedral phase coexistence for $x = 0.05$. On further increasing Sn(x) content, the characteristic peak of the rhombohedral phase present around 106 cm^{-1} becomes more pronounced with the existence of triple mode (E[TO1], A_1[LO], A_1[TO1]), which confirms a rhombohedral phase for $x = 0.075$, in agreement with the dielectric studies. The earlier studies performed on $Ba(Sn_xTi_{1-x})O_3$ show a cubic phase for higher Sn(x) content [166]. In Raman spectroscopic studies, the cubic phase of perovskite is characterized by the presence of two broad bands around 250 and 520 cm^{-1} [204, 227]. Moreover, the peak present around 719 cm^{-1} and the dip around 176 cm^{-1} observed in the tetragonal phase disappears in the cubic phase [204, 227]. The peak situated around 300 cm^{-1} (signature of the ferroelectricity [267]) has shown a nearly vanishing character for $x = 0.10$ and seems to have been merged with the one corresponding to A_1[TO2] phonon modes, similar as previously reported in $Ba(Zr_xTi_{1-x})O_3$ ceramics [189]. The spectra for $x = 0.10$ clearly show some peaks rather than a single band around 250 cm^{-1} (see Fig. 5.4), indicating some additional phase in contrast to the cubic one. Also, the temperature-dependent dielectric studies have inferred that the cubic to rhombohedral phase transition for $x = 0.10$ is lying in the vicinity of room temperature. Thus the analysis reveals a two-phase (cubic+rhombohedral) coexistence for $x = 0.10$.

5.3.4 X-ray diffraction studies

The preliminary investigation about the various crystallographic structural phase transitions present in BCZTSnx ceramics has been done by visually inspecting the evolution of the X-ray diffraction peaks corresponding to $\{h00\}$, $\{hh0\}$ and $\{hhh\}$ reflections. Fig. 5.5 depicts the evolution of peaks corresponding to (200), (220), and (222) reflections for

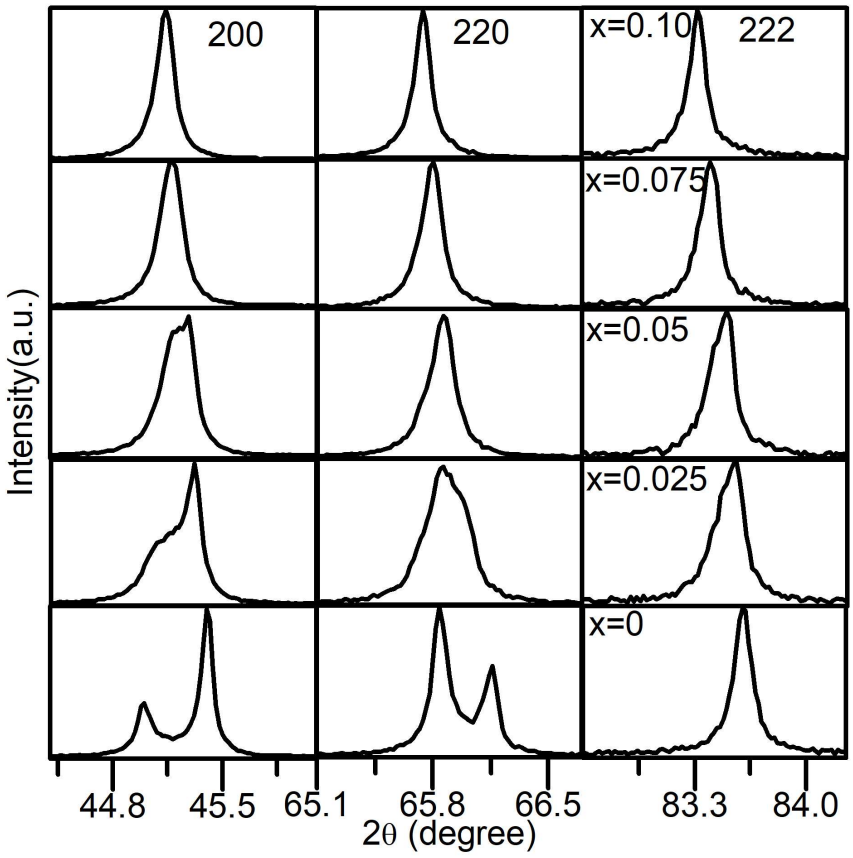

Fig. 5.5 Evolution of 200, 220, and 222 peaks profiles for BCZTSnx ($0 \leq x \leq 0.10$) ceramics.

BCZTSnx ceramics. The peaks show a shift towards lower 2θ angles because of the replacement of smaller ionic radii cation Ti^{4+}(61 pm), with larger ionic radii cation Sn^{4+}(69 pm) at the 'B' site. It is clearly evident from Fig. 5.5 that various new feature appears as a function of Sn(x) content dictating the presence of composition-dependent crystallographic structural phase transitions. For x = 0, the peak profiles correspond to the room temperature tetragonal phase of $BaTiO_3$ [161]. For higher compositions, *i.e.,* x = 0.025 and x = 0.05, the peaks have shown further splitting and broadening. Moreover, for x = 0.075 and 0.10, the peaks have exhibited some asymmetric nature. Generally, in tetragonal phase the peak corresponding to $\{h00\}$, and $\{hh0\}$ reflections splits into two, while the peaks corresponding to $\{hhh\}$ reflections show a non-split character. In the

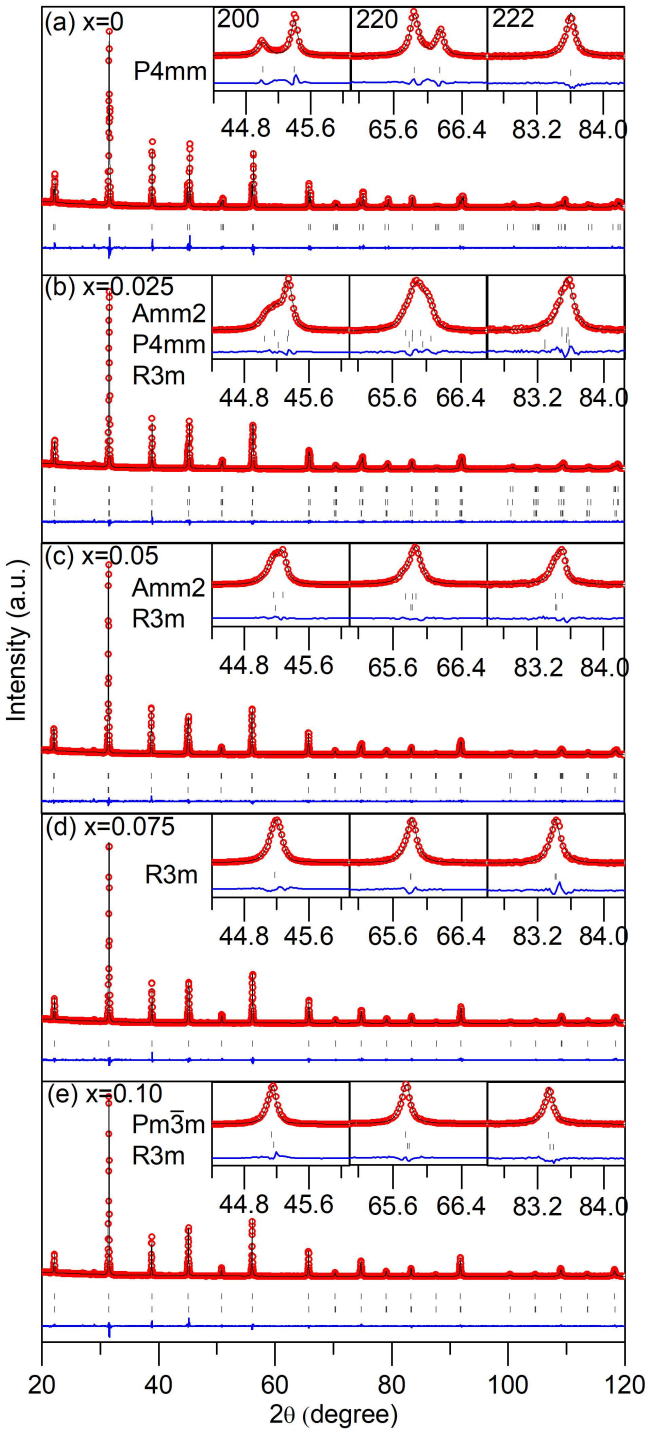

Fig. 5.6 Rietveld fitted X-ray diffraction peak profiles for BCZTSnx ($0 \leq x \leq 0.10$) ceramics. For each panel, the observed pattern is represented by the open (red) circles, the simulated pattern is represented via continuous (black) lines, the vertical lines (gray) correspond to the Bragg reflections, while the continuous horizontal line (blue) below the vertical bars corresponds to the difference between the observed and simulated patterns.

orthorhombic phase, the peak corresponding to $\{hhh\}$ reflections show a similar nature to that of the tetragonal phase, while the peaks associated with $\{h00\}$, and $\{hh0\}$ reflections split into three. Further, in rhombohedral phase, the peak associated with $\{h00\}$ reflection remains single, while one corresponding to $\{hh0\}$ and $\{hhh\}$ reflections split into two. The observed X-ray diffraction peak profile for x=0 clearly shows the characteristic peak splitting of a tetragonal phase. The dielectric and Raman spectroscopic studies also demonstrate a tetragonal phase for $x = 0$. Thus the single-phase tetragonal ($P4mm$) model has been considered for the Rietveld refinements, which provides a satisfactory fit with reasonable agreement factors (see Fig. 5.6(a) and Table 5.2). However, for $x = 0.025$, the (200) peak is splitted in more than two, (220) peak shows a significant broadening, and the (222) peak is asymmetric in nature. Thus the peak profile indicates a structural phase transition at $x = 0.025$, which may have coexisting phases. The temperature-dependent dielectric study shows that the tetragonal to orthorhombic phase transition for $x = 0.025$ lie in the vicinity of room temperature, while Raman spectroscopic studies exhibit the signature of the rhombohedral phase. The previous studies on $Ba(Sn_xTi_{1-x})O_3$ have observed the stabilization of low symmetry $Amm2$ and $R3m$ phases at room temperature (compatible with that of $BaTiO_3$) with a slight increase in Sn(x) content [8]. Thus different plausible models, *viz.,* (i) $P4mm$, (ii) $Amm2$ (iii) $P4mm + R3m$ (iv) $Amm2 + R3m$ (v) $P4mm + Amm2$ have been tried for the Rietveld refinement of the diffraction data for $x = 0.025$ (see Fig.

Table 5.2 Structural parameters and various agreement factors obtained from the Rietveld refinements of the X-ray diffraction patterns for $x = 0$ via single-phase ($P4mm$) model.

Space group: $P4mm$				
Atoms	x	y	z	U(Å^2)
Ba/Ca	0.000	0.000	0.000	0.0039(3)
Ti/Sn/Zr	0.500	0.500	0.481(3)	0.0042(9)
O_1	0.500	0.500	0.025(11)	0.001(4)
O_2	0.500	0.000	0.486(9)	0.005(3)
a = 3.99235(6) Å, c = 4.02470(8) Å, v = 64.149(2) Å^3				
Agreement factors: R_{wp} = 10.02, R_{exp} = 6.01, χ^2 = 2.89				

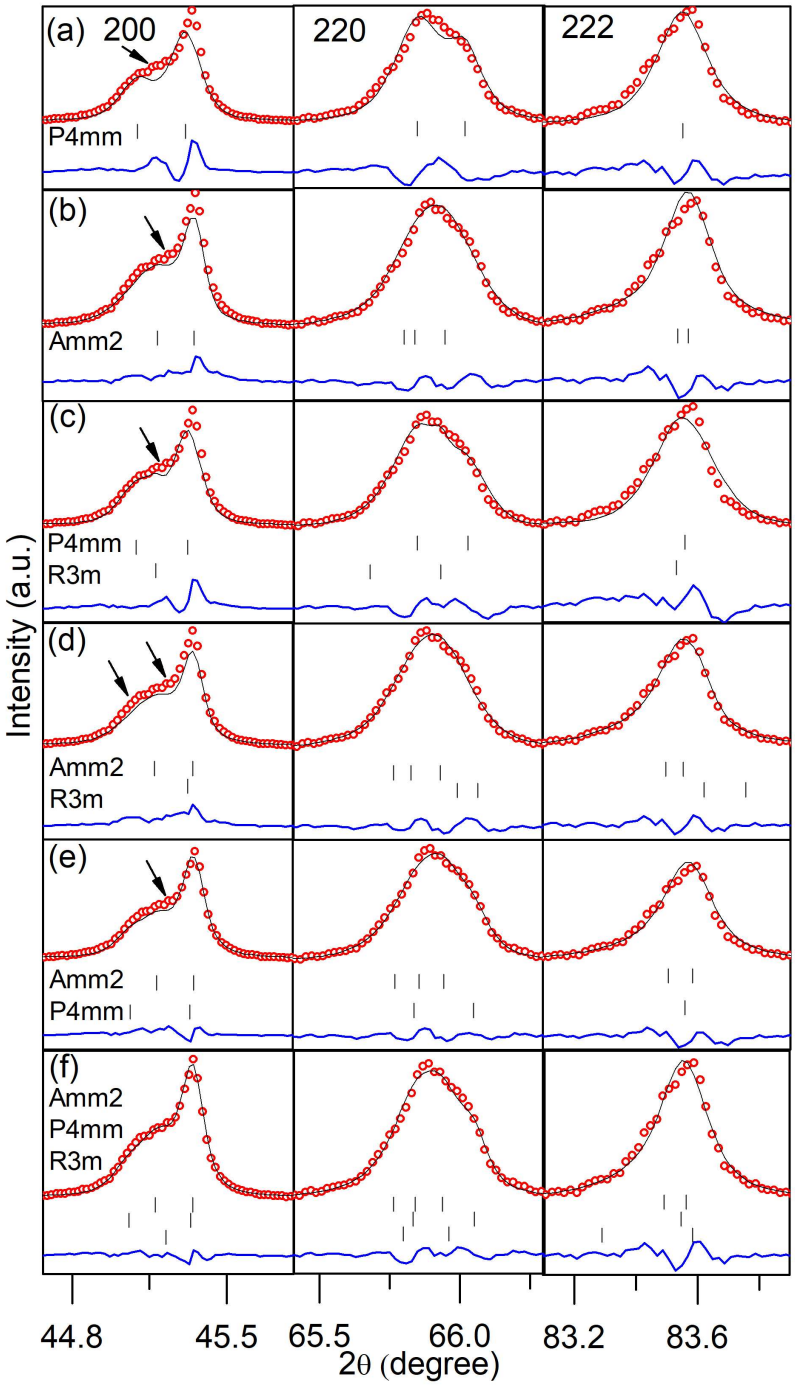

Fig. 5.7 Rietveld fitted X-ray diffraction peak profile evolution corresponding to 200, 220, and 222 reflections for $x = 0.025$, via (a) $P4mm$ (b) $Amm2$ (c) $P4mm + R3m$ (d) $Amm2 + R3m$ (e) $P4mm + Amm2$, and (f) $P4mm + Amm2 + R3m$ models. The arrow mark indicates the peaks that could not be indexed using the particular model.

5.7). The fitting performed with various models, *viz.,* (i) *P*4*mm* ($R_{\rm wp}$ = 10.2, R_{exp} = 6.25 & χ^2 = 2.64), (ii) *Amm*2 ($R_{\rm wp}$ = 8.60, $R_{\rm exp}$ = 6.25 & χ^2 = 1.89) (iii) *P*4*mm* + *R*3*m* ($R_{\rm wp}$ = 9.32, $R_{\rm exp}$ = 6.25 & χ^2 = 2.23) (iv) *Amm*2 + *R*3*m* ($R_{\rm wp}$ = 8.39, $R_{\rm exp}$ = 6.24 & χ^2 = 1.81) (v) *P*4*mm* + *Amm*2 (R_{wp} = 7.92, R_{exp} = 6.23 & χ^2 = 1.62) were unable to provide a good fit of the data. However, among the above-mentioned models, the refinement performed with the model (v) *P*4*mm* + *Amm*2, was the best one, but still, all the features present in the peak profile could not be appropriately taken into account (shown by the arrow mark in Fig. 5.7(e)). Thus, in line with the combined dielectric and Raman spectroscopic studies, a three-phase model, *viz.,* model (vi) *P*4*mm* + *Amm*2 + *R*3*m* has been used, and the refinement has led to a best fit having good agreement factors (R_{wp} = 7.42, R_{exp} = 6.23 & χ^2 = 1.42) among all the tried models (see Fig. 5.6(b) and Table 5.3). A similar three-phase (*P*4*mm* + *Amm*2 + *R*3*m*) coexistence has been recently reported by Brajesh *et al.* in the widely explored (Ba,Ca)(Zr,Ti)O_3 ceramic system. Brajesh *et al.* found that among the three phases, the *P*4*mm* phase was the dominating one [193], as observed for x = 0.025 in BCZTSnx ceramics. However, Brajesh *et al.* reported that the fraction of the *Amm*2 phase was smaller than the *P*4*mm* phase, but it was more than the *R*3*m* phase [193], but for x = 0.025, although the fraction of both the *Amm*2 (5.23%) and *R*3*m* (13.41%) phases is smaller than the *P*4*mm* (81.36%) phase, but among the *Amm*2 and *R*3*m* phases, the *R*3*m* has a larger phase fraction. Here, it is worthy to note that the fraction of the *R*3*m* phase is larger than the *Amm*2 phase, which indicates that the propensity of transforming the ⟨100⟩ (tetragonal) polarization state (present in x = 0), into ⟨111⟩ (rhombohedral) polarization state is more than the ⟨110⟩ (orthorhombic) state for x = 0.025. Moreover, Brajesh *et al.* argued that the high piezoresponse and ferroelectric polarization of (Ba,Ca)(Zr,Ti)O_3 ceramics is mainly attributed to off-centered Ti^{4+} cations and the propensity of transformation from ⟨100⟩ to ⟨111⟩ polarization state rather than ⟨110⟩ on the application of electric field [193]. Thus, the transformation of the polarization state

Table 5.3 Structural parameters, phase fraction, and various agreement factors obtained from the Rietveld refinements of the X-ray diffraction patterns for $x = 0.025$ via three-phase ($P4mm + Amm2 + R3m$) coexistence model.

Atoms	x	y	z	U(Å^2)
Space group: $P4mm$				
Ba/Ca	0.000	0.000	0.000	0.0052(11)
Ti/Sn/Zr	0.500	0.500	0.489(13)	0.008(3)
O_1	0.500	0.500	0.01(5)	0.007(10)
O_2	0.500	0.000	0.48(2)	0.003(7)
a = 3.99751(11) Å, c = 4.02096(18) Å, v = 64.255(4) Å^3				
Phase fraction = 81.36%				
Space group: $Amm2$				
Ba/Ca	0.000	0.000	0.000	0.0011(10)
Ti/Sn/Zr	0.500	0.000	0.507(13)	0.003(3)
O_1	0.000	0.000	0.52(2)	0.003(10)
O_2	0.500	0.266(17)	0.25(2)	0.000(7)
a = 3.99648(7) Å, b = 5.66928(22) Å, c = 5.67537(34) Å, v = 128.588(9) Å^3				
Phase fraction = 5.23%				
Space group: $R3m$				
Ba/Ca	0.000	0.000	0.000	0.009(15)
Ti/Sn/Zr	0.000	0.000	0.50(14)	0.00(3)
O	0.17(7)	0.33(7)	0.30(14)	0.00(13)
a = 5.660(3) Å, c = 6.955(7) Å, v = 192.96(30) Å^3				
Phase fraction=13.41%				
Agreement factors: R_{wp} = 7.42, R_{exp} = 6.23, χ^2 = 1.42				

from $\langle 100 \rangle$ to $\langle 111 \rangle$ state with an increase in Sn(x) content of BCZTSnx ceramics is similar to the field-induced phase transition behaviour of (Ba,Ca)(Zr,Ti)O_3 [193]. Therefore, based on the above analysis, it is reasonable to argue that $x = 0.025$ ceramics may be a potential candidate for various piezoelectric applications. On further increasing Sn(x) content, the peak corresponding to (200) and (222) reflections splits into two. The splitting of the (222) peak depicts the appearance of a rhombohedral phase, but the splitting of the (200) peak has directed us to a phase coexistence for $x = 0.05$, as depicted by combined dielectric and Raman spectroscopic studies. Thus, a two-phase ($Amm2 + R3m$) model has been considered for the Rietveld refinement, which gives a satisfactory fit with agreement factors (R_{wp} = 7.54, R_{exp} = 6.04 & χ^2 = 1.56) having reasonable values (see Fig. 5.6(c)

Table 5.4 Structural parameters, phase fraction, and various agreement factors obtained from the Rietveld refinements of the X-ray diffraction patterns for $x = 0.05$ via two-phase ($Amm2 + R3m$) coexistence model.

Atoms	x	y	z	U(Å^2)
Space group: $Amm2$				
Ba/Ca	0.000	0.000	0.000	0.0028(4)
Ti/Sn/Zr	0.500	0.000	0.510(4)	0.0042(10)
O_1	0.000	0.000	0.51(3)	0.005(6)
O_2	0.500	0.268(10)	0.252(10)	0.001(4)
a = 4.00236(5) Å, b = 5.66975(17) Å, c = 5.67660(18) Å, v = 128.816(6) Å^3				
Phase fraction = 11.03%				
Space group: $R3m$				
Ba/Ca	0.000	0.000	0.000	0.0092(15)
Ti/Sn/Zr	0.000	0.000	0.476(7)	0.004(7)
O	0.153(14)	0.306(14)	0.330(7)	0.000(7)
a = 5.6712(3) Å, c = 6.9447(6) Å, v = 193.43(2) Å^3				
Phase fraction=88.97%				
Agreement factors: R_{wp} = 7.54, R_{exp} = 6.04, χ^2 = 1.56				

and Table 5.4). However, to avoid any sort of ambiguity, we have also tried the structural refinement with single phase orthorhombic ($Amm2$) model since the orthorhombic ($Amm2$) to rhombohedral ($R3m$) phase transition peak in the real part of the dielectric constant plot lies in the vicinity of room temperature. The refinement performed with the single-phase $Amm2$ model was unable to include all the features present in the peak profile (see Fig. 5.8), and the obtained agreement factors (R_{wp} = 8.82, R_{exp} = 6.04 & χ^2 = 2.13) have relatively higher values than the two-phase ($Amm2 + R3m$) model. The phase fraction of

Table 5.5 Structural parameters and various agreement factors obtained from the Rietveld refinements of the X-ray diffraction patterns for $x = 0.075$ via single-phase ($R3m$) model.

Atoms	x	y	z	U(Å^2)
Space group: $R3m$				
Ba/Ca	0.000	0.000	0.000	0.0052(4)
Ti/Sn/Zr	0.000	0.000	0.515(4)	0.003(2)
O	0.181(6)	0.361(6)	0.333(3)	0.000(3)
a = 5.6711(1) Å, c = 6.9467(2) Å, v = 193.48(1) Å^3				
Agreement factors: R_{wp} = 8.66, R_{exp} = 6.26, χ^2 = 1.91				

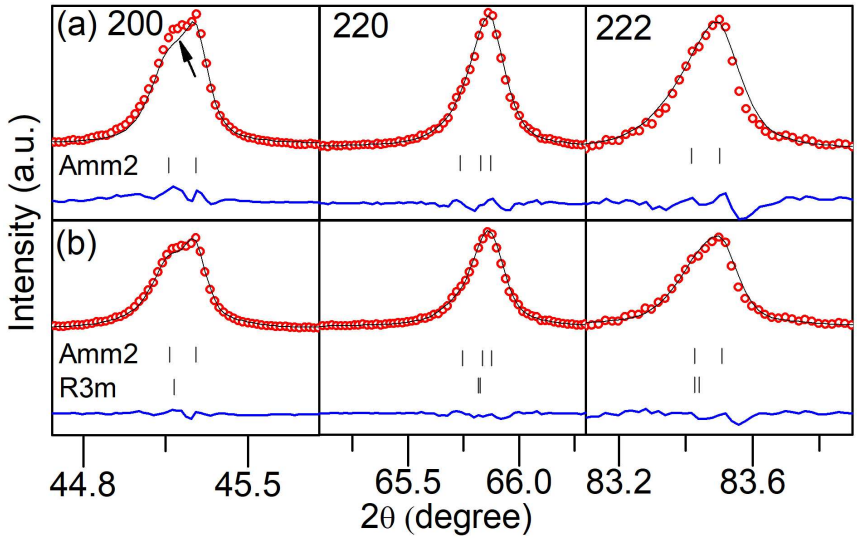

Fig. 5.8 Rietveld fitted X-ray diffraction peak profile evolution corresponding to 200, 220, and 222 reflections for $x = 0.05$, via (a) $Amm2$ and (b) $Amm2 + R3m$ models. The arrow mark indicates the peak that could not be indexed using the particular model.

the $Amm2$ (11.03%) phase in $x = 0.05$ was found to be significantly smaller than that of the $R3m$ (88.97%) phase, which further indicates that the $\langle 100 \rangle$ (tetragonal) polarization state (present in $x = 0.025$) has shown more propensity towards $\langle 111 \rangle$ (rhombohedral) polarization state, rather than $\langle 110 \rangle$ (orthorhombic) polarization state. Therefore, we see that the increase in Sn(x) content is favouring the stabilization of the low symmetry polarization state, *viz.,* $\langle 111 \rangle$, compatible with the low temperature rhombohedral ($R3m$) phase of $BaTiO_3$. Further, for higher composition, *i.e.,* $x = 0.075$, the (200), (220), and (222) peaks show an asymmetric nature. The dielectric and Raman spectroscopic studies suggest a rhombohedral phase for $x = 0.075$. Thus, a single-phase rhombohedral ($R3m$) model was used for the refinement, and the model has given a satisfactory fit ($R_{wp} = 8.66$, $R_{exp} = 6.26$ & $\chi^2 = 1.91$), indicating a rhombohedral ($R3m$) phase for $x = 0.075$ (see Fig. 5.6(d) and Table 5.5). Finally, for $x = 0.10$, we have used a two-phase ($Pm\bar{3}m$+$R3m$) model, as per the combined dielectric and Raman spectroscopic studies. The model gives a good

Table 5.6 Structural parameters, phase fraction, and various agreement factors obtained from the Rietveld refinements of the X-ray diffraction patterns for $x = 0.10$ via two-phase ($Pm\bar{3}m$+$R3m$) coexistence model.

Atoms	x	y	z	U(Å^2)
		Space group: $Pm\bar{3}m$		
Ba/Ca	0.000	0.000	0.000	0.0034(4)
Ti/Sn/Zr	0.500	0.500	0.500	0.0042(7)
O	0.500	0.500	0.000	0.0044(17)
		$a = 4.01372(2)$ Å, $v = 64.661(1)$ Å^3		
		Phase fraction = 86.51%		
		Space group: $R3m$		
Ba/Ca	0.000	0.000	0.000	0.011(5)
Ti/Sn/Zr	0.000	0.000	0.514(16)	0.008(12)
O	0.15(4)	0.30(4)	0.317(18)	0.00(3)
		$a = 5.6728(2)$ Å, $c = 6.9509(2)$ Å, $v = 193.72(1)$ Å^3		
		Agreement factors: $R_{wp} = 9.02$, $R_{exp} = 6.06$, $\chi^2 = 2.21$		
		Phase fraction = 13.49%		

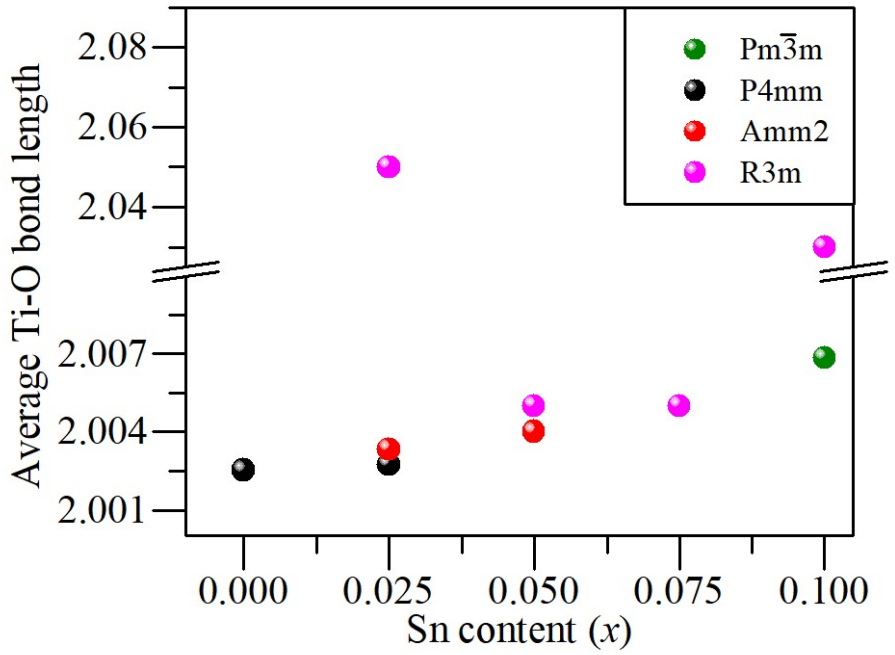

Fig. 5.9 Variation of average Ti-O bond length corresponding to cubic ($Pm\bar{3}m$), tetragonal ($P4mm$), orthorhombic ($Amm2$), and rhombohedral ($R3m$) phases for BCZTSnx ($0 \leq x \leq 0.10$) ceramics.

Table 5.7 Composition-dependent variations of Ti-O bond lengths (in Å) for BCZTSnx ($0 \leq x \leq 0.10$) ceramics.

Bond lengths/Space group					
$x = 0$					
Bond lengths	*P*4*mm*				
Ti—O1	1.84				
Ti—O1	2.19				
Ti—O2x2	1.9963				
Ti—O2x2	1.9963				
Average	2.0025				
$x = 0.025$					
Bond lengths	*P*4*mm*	Bond lengths	*Amm*2	Bond lengths	*R*3*m*
Ti—O1	1.93	Ti—O1	2.000	Ti—O1x3	2.2
Ti—O1	2.09	Ti—O1	2.000	Ti—O2x3	1.9
Ti—O2x2	1.9991	Ti—O2x2	2.09		
Ti—O2x2	1.9991	Ti—O2x2	1.92		
Average	2.0027	Average	2.0033	Average	2.05
$x = 0.05$					
Bond lengths	*Amm*2	Bond lengths	*R*3*m*		
Ti—O1	2.002	Ti—O1x3	2.21		
Ti—O1	2.002	Ti—O2x3	1.80		
Ti—O2x2	2.11				
Ti—O2x2	1.90				
Average	2.004	Average	2.005		
$x = 0.075$					
Bond lengths	*R*3*m*				
Ti—O1x3	2.19				
Ti—O2x3	1.82				
Average	2.005				
$x = 0.10$					
Bond lengths	$Pm\bar{3}m$	Bond lengths	*R*3*m*		
Ti—Ox6	2.00686	Ti—O1x3	2.04		
		Ti—O2x3	2.02		
Average	2.00686	Average	2.03		

quality of fit (see Fig. 5.6(e) and Table 5.6) and reasonable agreement factors (R_{wp} = 9.02, R_{exp} = 6.06 & χ^2 = 2.21), confirming a $Pm\bar{3}m$+*R*3*m* phase coexistence, with the fractions of phases being 86.51% and 13.49%, respectively. The coexistence of $Pm\bar{3}m$ and *R*3*m* phases for x = 0.10 is similar to one reported in $Ba(Sn_xTi_{1-x})O_3$ ceramics, for higher Sn(x)

compositions, before transforming the system into a single cubic ($Pm\bar{3}m$) phase [166]. The presence of several crystallographic phase transitions as a function of Sn(x) has also been supported by the appearance of anomalies in variations of average Ti-O bond length at the phase transitions (see Table 5.7 and Fig. 5.9).

5.3.5 Symmetry mode analysis

Around 1960, it was predicted independently by Anderson and Cocharan that the origin of ferroelectric phase transitions lies in the soft modes, *i.e.,* in the lattice instabilities [100]. The soft modes are generally defined as the collective excitations which show an anomalous decrease in frequency as the phase transition is reached [271]. In ferroelectrics, the spontaneous polarization arises due to the shift of positive charges with respect to negative charges. Such displacements correspond to the similar movement of ions as the zone center transverse optical phonon mode termed as soft mode [272]. It is well known that several ferroelectric materials exhibit a divergent dielectric constant. The lattice dynamics studies have predicted that the dielectric constant varies inversely to that of the square of the frequency of a transverse optic mode of vibration as given below [273],

$$\varepsilon^{'} \approx \frac{C}{(T - T_c)} \approx \frac{M^2}{\omega(0)^2} \tag{5.1}$$

Here C represents the Curie constant, and M is the dipole moment of the transverse optic vibration mode. Hence the frequency of the soft mode can be represented as

$$\omega(0)^2 \approx (T - T_c) \tag{5.2}$$

This equation shows that the frequency of the soft mode decreases with the lowering of temperature, and when the Curie temperature is reached, it tends to zero, and the mode gets frozen, leading to a transformation into a ferroelectric phase. The freezing of the

mode leads to a non-zero order parameter, and a reduction in symmetry [19]. Thus the low symmetry phase is regarded as a distorted phase with respect to the high symmetry one. Here, the 'distortion' corresponds to the set of structural degrees of freedom in the low-symmetry phase, resulting due to a phase transition [274]. The distortion symmetry is described uniquely with the three things, *viz.,* a 'k' point, an irrep, and one of its order parameter directions (OPD). Generally, the space group irreps are defined with respect to a particular reciprocal space 'k' point, and the irrep belonging to the parent space group can only lead to the structural distortions that generate the reciprocal lattice defined by its 'k' point [274]. Here, the OPD is a direction in the carrier space of the irrep, and every distinct vector in such a subspace represents a different direction. Further, in this scenario, the order parameter (ξ) is defined as a vector in distortion space that lies along a specific OPD of a specific irrep at a specific 'k' point [274]. In general, the distorted structure contains a primary component corresponding to the mode(s), which are unstable in high symmetry structure [266]. The primary nature of the order parameter means that it can energetically drive the phase transition, and the irreps which induce the primary order parameter are called the primary irrep. The distortions may also contain other secondary order parameters (irreps), which can cooperate with the primary order parameter and freezes through the coupling with the primary order parameter. The distortion modes corresponding to the primary order parameters can always independently lead to the final distortion symmetry. On the other hand, the secondary order parameters are usually insufficient to lower the symmetry [274]. However, in some cases, the secondary order parameters are sufficient to break the symmetry of the parent structure. Let such a secondary order parameter is represented by ξ_2. If ξ_1 corresponds to the primary order parameter, then ξ_2 will be coupled with ξ_1 as the secondary order parameter. However, if ξ_2 acts as a primary order parameter, then ξ_1 will be coupled with ξ_2 as the secondary order parameter [274]. Moreover, in some of the cases, the distorted structure can not be generated via a

single primary order parameter, and the simultaneous coupling of multiple primary order parameters is required for the distorted phase. This phenomenon does not lead to any additional distortion modes, but the combination of the existing modes corresponding to different irreps leads to relatively more complex distortions [274]. Further, the distortion modes corresponding to the different irreps of the parent structure have generally distinct origins, and therefore they exhibit different behaviours when subjected to any external perturbations. From the crystallographic structural point of view, the description of the structures in terms of the symmetry-adapted modes can be very useful for comparing the behaviour of different structures of the same material or different materials having similar structures [266]. The contribution of the different modes in the structural distortions is generally achieved by the technique so-called symmetry mode analysis. In this work, we have performed the symmetry mode analysis of BCZTSnx ceramics to quantify the relative intrinsic contribution of the ferroelectricity for different compositions.

The symmetry mode analysis is based on the application of group theory in solid-state physics. The symmetry mode analysis can be performed using AMPLIMODES [265, 266], and ISODISTORT [274, 275] software. In this study, we have used the AMPLIMODES software to analyse the structural distortions. As we know that many of the crystallographic structures exhibited by different materials can be considered as a distorted phase with respect to some high symmetry parent structure. The parent structure with respect to which the distorted phase is going to be described may be some high-symmetry phase of that system, or it may be some virtual parent structure, provided that the distorted structure should be a subgroup of the high-symmetry one. Let us consider G as the space group of the parent structure, H represents the space group of the low symmetry distorted phase, and the symmetry breaking takes place as G$\rightarrow$H. Then the transformation from the conventional bases of G to H given by $(a,b,c)_{\mathrm{G}}$ and $(a,b,c)_{\mathrm{H}}$ respectively, is described as

$$(a,b,c)_{\mathrm{H}} = (a,b,c)_{\mathrm{G}}P \tag{5.3}$$

Here P is called the transformation matrix, corresponding to a transformation from the conventional basis of G to the conventional basis of H. In this way, the low symmetry distorted structure is considered as the parent structure subjected to a static symmetry-breaking structural distortion. Let $r_0(n, j)$ represents the atomic positions of the n atoms in the asymmetric unit of the parent structure having space group G. The low symmetry structure having space group H, which is a subgroup of G, generally has greater number of atoms within the asymmetric unit due to the wyckoff site splitting of the parent structure. Thus the atomic positions within the asymmetric unit H may be represented by the following relation

$$r(n, j) = r_0(n, j) + u(n, j) \tag{5.4}$$

where, the $r(n, j)$ represents the positions of the atoms within the H asymmetric unit, and $u(n, j)$ corresponds to the atomic displacements within the asymmetric unit of the low symmetry distorted phase. Here, the label j denotes that the wyckoff sites of the space group H are arising from the unique site of G. The amplitude of the displacement gives rise to the magnitude of displacive distortion. Thus we see that the initial things required to perform the symmetry mode analysis is a high-symmetry parent structure, the lattice parameters, atomic coordinates and the space group of the low-symmetry phase, a transformation matrix that relates the high-symmetry parent structure to the low symmetry distorted phase, and the polarization vector belonging to the respective distortion mode responsible for quantifying the atomic displacements contribution in the overall distortion [276]. Using these information the output in the AMPLIMODES gives rise to the amplitudes of each of the distortion mode(s). In the context of phase transitions, these amplitudes act as order parameter components, and any arbitrary distortions can be decomposed into various involved distortion modes (each allied with one of structural degree of freedom) whose amplitude gives rise their contributions in overall atomic displacement pattern [274].

In order to quantify the relative magnitude of ferroelectricity in BCZTSnx ceramics, we have carried out symmetry mode analysis using 'AMPLIMODES' software available on Bilbao crystallographic server [265, 266]. We have chosen the $P\bar{3}$m (a = 4.013725 Å) phase of x = 0.10, as a common reference. The origin was selected at A(Ba/Ca) site atom located at '1a' wyckoff position having positional coordinates (0,0,0), whereas B(Ti/Sn/Zr) site and O atoms are located at ($\frac{1}{2}$,$\frac{1}{2}$,$\frac{1}{2}$) and ($\frac{1}{2}$,$\frac{1}{2}$,0), corresponding to '1b' and '3c' wyckoff position, respectively. The mode amplitudes have been calculated using the lattice parameters and positional coordinates obtained from the Rietveld refinements of the room-temperature powder X-ray diffraction data. The Rietveld refinement of the diffraction data of BCZTSnx ceramics has revealed the presence of all the crystallographic structures consistent with the temperature-dependent phase diagram of $BaTiO_3$. Out of them, the tetragonal ($P4mm$) phase results due to component freezing of Γ_4^- phonon mode (three-dimensional in nature), leading to a ferroelectric displacement along $\langle 001 \rangle$ direction. To observe the splitting of wyckoff positions corresponding to high symmetry ($Pm\bar{3}m$) space group via symmetry reduction into its subgroup, we have used the 'WYCKSPLIT' program [277], and the irreps of the possible active modes have been found via 'SYMMODES' tool available at Bilbao crystallographic server [278]. In the $P4mm$ phase, the '1a' and '1b' site of high symmetry cubic ($Pm\bar{3}m$) phase transforms into '1a' and '1b' site of tetragonal phase, whereas '3c' site splits into '2c' and '1b' sites, via Γ_4^- distortion mode(s). Thus, the $P4mm$ phase results due to the freezing of one Γ_4^- distortion mode associated with the 'A' site atom, one with the 'B' site atom, whereas two Γ_4^- modes associated with the oxygen atoms of the high symmetry cubic phase. On the other hand, the rhombohedral ($R3m$) phase results due to freezing of Γ_4^- phonon mode, leading to polar displacement along $\langle 111 \rangle$ direction. Here, both '1a' and '1b' sites corresponding to the $Pm\bar{3}m$ phase, transforms into a '3a' wyckoff site of the $R3m$ phase via a Γ_4^- distortion mode, whereas the '3c' site transforms into '9b' site via two Γ_4^- distortion modes. Furthermore, the

Table 5.8 Amplitude of the phonon mode(s) in low symmetry ferroelectric phases of BCZTSnx ceramics, with respect to high symmetry cubic ($Pm\bar{3}m$) phase.

Composition (x)	Phase	Irrep	OPD	Amplitude (Å)
0	$P4mm$	Γ_4^-(T)	(0,0,a)	0.1436
0.025	$P4mm$	Γ_4^-(T)	(0,0,a)	0.0914
	$Amm2$	Γ_4^-(O)	(a,a,0)	0.1703
		Γ_5^-(O)	(0,a,-a)	0.0225
	$R3m$	Γ_4^-(R)	(a,a,a)	0.2744
0.05	$Amm2$	Γ_4^-(O)	(a,a,0)	0.1434
		Γ_5^-(O)	(0,a,-a)	0.0578
	$R3m$	Γ_4^-(R)	(a,a,a)	0.2672
0.075	$R3m$	Γ_4^-(R)	(a,a,a)	0.2558

distortions corresponding to orthorhombic ($Amm2$) phase can be decomposed into two distinct modes, *viz.,* Γ_4^- and Γ_5^-. Here, Γ_4^- mode is associated with the polar displacement of the ferroelectrically active 'B' site cation, leading to polarization along $\langle 110 \rangle$ direction, whereas Γ_5^- is a nonpolar distortion mode which leads to antiferroelectric displacements averse to the ferroelectric one [14, 94]. Moreover, using 'ISOSUBGROUP' software [275, 279], we have found that the $Amm2$ phase can be achieved due to freezing of any one of these two modes, *viz.,* Γ_4^- or Γ_5^-, or by their coupling, where the primary phonon mode needs to be identified based on the relative amplitudes of the distortion modes. If the amplitude of Γ_4^- is larger than that of Γ_5^-, then Γ_4^- will act as a primary order parameter and Γ_5^- will be the secondary one, and consequently, the $Amm2$ phase is termed as a proper ferroelectric, whereas if Γ_5^- phonon mode has a larger amplitude than the Γ_4^-, then Γ_5^- will be the primary order parameter and the $Amm2$ will be termed as improper ferroelectric. Nonetheless, the $Amm2$ phase is characterized by a total of five ($4\Gamma_4^-$+Γ_5^-) distortion modes. Here, the '1a' and '1b' site of the $Pm\bar{3}m$ phase transforms into '2a' and '2b' site, each via a Γ_4^- distortion mode, and the '3c' site of the $Pm\bar{3}m$ phase get split into '4e' and '2a' wyckoff sites via two Γ_4^- and one Γ_5^- distortion modes. Thus the single Γ_5^- phonon mode is associated with the displacement of the oxygen atom. In addition to Γ_5^- phonon mode, two Γ_4^- modes also corresponds to the oxygen atoms, and 'A', as well as 'B' site atoms are allied

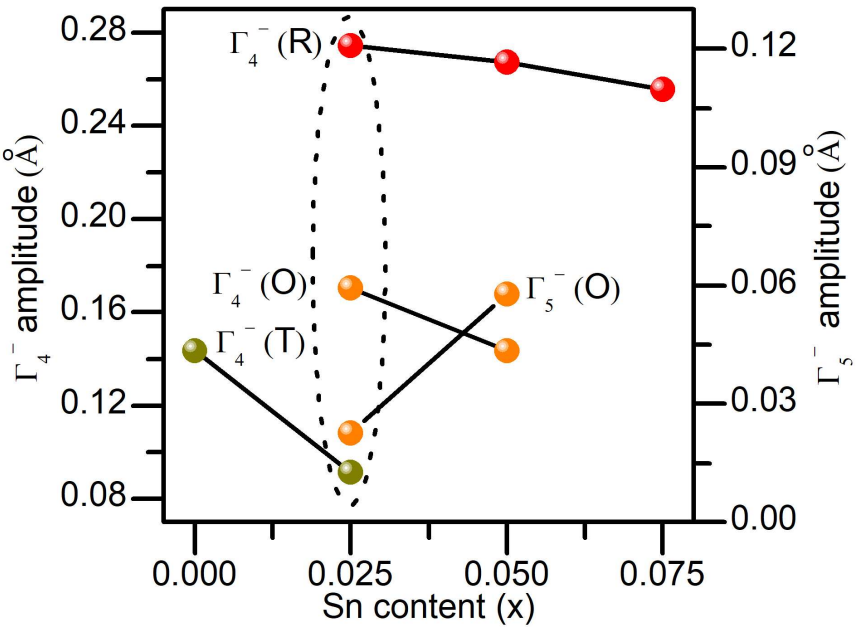

Fig. 5.10 Variation in amplitude of polar (Γ_4^-) and nonpolar (Γ_5^-) phonon mode for BCZTSnx ceramics as a function of Sn(x) content.

with one Γ_4^- phonon mode. The calculated amplitudes of the distortion modes are listed in Table 5.8. One can see that with the increase in Sn(x) content, the amplitude of Γ_4^- phonon mode associated with the *P*4*mm* phase, *i.e.,* Γ_4^-(T) decreases, whereas the amplitudes of the ferroelectric phonon modes, *viz.,* Γ_4^-(O) and Γ_4^-(R) corresponding to additional *Amm*2 and *R*3*m* phases for x = 0.025 (which were absent in x = 0), have shown the highest value among the fabricated compositions. The X-ray diffraction studies have also demonstrated a decrease in the tetragonality ratio from η = 0.0081 (x = 0) to η = 0.0058 (x = 0.025), consistent with the decrease in amplitude of ferroelectric Γ_4^-(T) distortion mode. The various atomic displacements pattern with respect to the cubic ($Pm\bar{3}m$) phase, leading to ferroelectrically distorted *P*4*mm*, *Amm*2, and *R*3*m* phases for x = 0.025, can be seen from Fig. 5.11. For x = 0.05, the amplitudes of the Γ_4^- phonon modes corresponding to orthorhombic and rhombohedral phases, *viz.,* Γ_4^-(O) and Γ_4^-(R), is lower than that of x = 0.025.

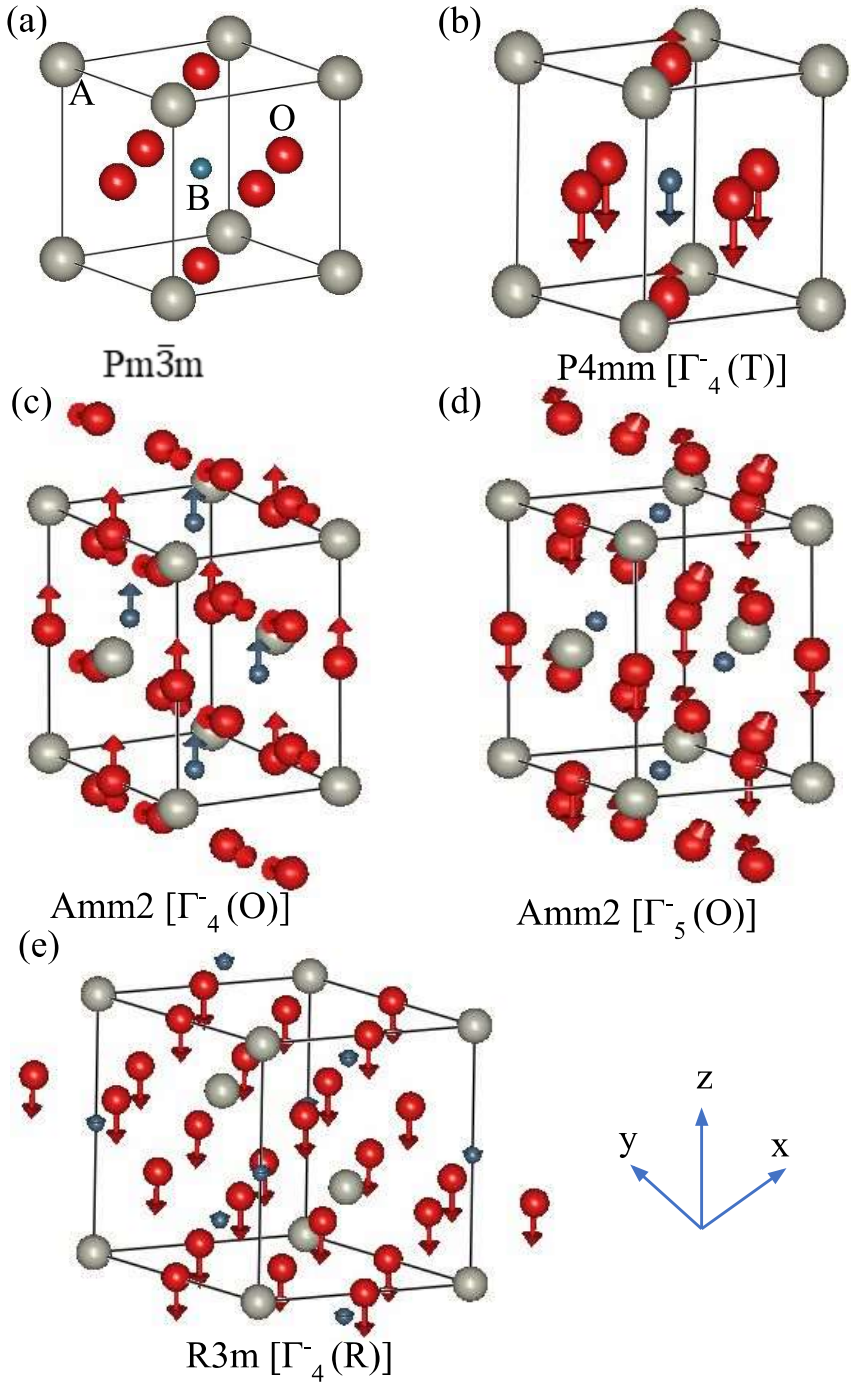

Fig. 5.11 Atomic displacements pattern for various ferroelectric phases of $x = 0.025$, driven by component(s) freezing of polar (Γ_4^-; involved in symmetry breaking to *P*4*mm*, *Amm*2, and *R*3*m* phases), and nonpolar (Γ_5^-; responsible for antiferroelectric displacements in *Amm*2 phase) zone center (k = 0,0,0) phonon modes belonging to the high symmetry cubic ($Pm\bar{3}m$) phase.

Interestingly the amplitude of the secondary antiferroelectric (nonpolar) phonon mode, *i.e.,* Γ_5^-(O) associated with the *Amm*2 phase, has shown a larger value for x = 0.05 than x = 0.025 (see Fig. 5.10), which indicates that the ferroelectric character of the ceramic composition x = 0.05 is lower than x = 0.025. However, corresponding to both the compositions, *viz.,* x = 0.025 and 0.05, the amplitude of Γ_4^-(O) phonon mode was found to be significantly larger than the Γ_5^-(O), which depicts the proper ferroelectric behaviour of the *Amm*2 phase for both these ceramic compositions. Further, for x = 0.075, the amplitude of the Γ_4^-(R) distortion mode is decreased, which shows that the intrinsic contribution in the ferroelectricity coming from the shift of ferroelectrically active cation is reduced with the increase in Sn(x) content.

5.3.6 Polarization *vs.* Electric field (PE) hysteresis loop analysis

To analyse the room temperature ferroelectricity in BCZTSnx ceramics, the polarization *vs.* electric field (PE) hysteresis loop measurement was carried out for all the compositions (see Fig. 5.12). The remnant polarization has shown a peak value (P_r = 4.97 μC/cm^2) for x = 0.025, and thereafter it has shown a decreasing trend (see inset of Fig. 5.12). The peaking behaviour of remnant polarization at x = 0.025 is attributed to the appearance of an inter-ferroelectric three-phase ($P4mm + Amm2 + R3m$) coexistence, distinct from the single tetragonal ($P4mm$) phase of x = 0. The studies performed in the past have demonstrated that the properties of the ceramics get enhanced at the multi-phase coexistence region due to easy polarization rotation resulting from the minimization of the energy barrier between the coexisting phases [38, 115]. The ease of polarization rotation phenomenon at the morphotropic phase boundary (MPB), leading to significantly enhanced properties, has been widely explored in Pb(Zr,Ti)O_3, where the MPB region comprises the tetragonal ($P4mm$) and rhombohedral ($R3m$) phases with a bridging monoclinic (Cm) phase [28, 38, 280]. Nonetheless, for x = 0.025, the ferroelectric contribution described in terms of the

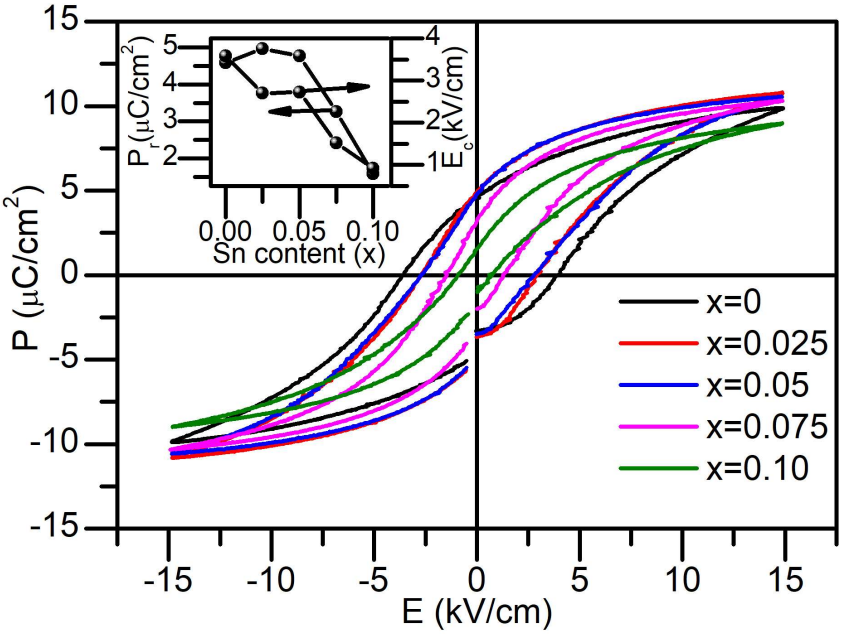

Fig. 5.12 Polarization vs. Electric field (PE) hysteresis loops for BCZTSnx $(0 \leq x \leq 0.10)$ ceramics measured at room temperature.

amplitude of Γ_4^- phonon mode has shown the highest value for *Amm*2 and *R*3*m* phases (see Fig. 5.10). However, the amplitude of Γ_4^-(T) mode was found to be smaller in $x = 0.025$ than $x = 0$, which is also corroborated by the decrease in tetragonality ratio of the *P*4*mm* phase for $x = 0.025$. Thus the high ferroelectric polarization of $x = 0.025$ is associated with the high amplitudes of the ferroelectric *Amm*2 and *R*3*m* phases around this composition and a probable easy polarization rotation phenomenon between the three (*P*4*mm*+*Amm*2+*R*3*m*) coexisting phases [38, 115]. On further increasing Sn(x) content, the polarization shows a decreasing trend which is attributed to the decreasing amplitudes of ferroelectric Γ_4^- phonon modes. Finally, for $x = 0.10$, the remnant polarization exhibits a minimum value, which is attributed to the appearance of a centrosymmetric $Pm\bar{3}m$ phase (fraction = 86.51%) for this composition. The coercive field (E_c) has shown an approximately decreasing trend with an increase in Sn(x) content. The decrease in the value of the coercive field suggests that the material is getting softer with respect to the electric field, as far as the Sn(x) concentration

is increasing. For x = 0.025, the E_c value is lower than x = 0, which is attributed to the multi-phase coexistence around this composition. Whenever a material undergoes a structural phase transition and transforms into a new phase having multi-phase coexistence region, the energy barrier between the coexisting phase gets significantly reduced in general, acquiring a low field for the polarization rotation, which reflects as a decrease in E_c value [204]. A similar phenomenon seems to happen in x=0.025 due to its three-phase ($P4mm + Amm2 + R3m$) coexistence. Interestingly, the value of coercive field (E_c = 2.70 kV/cm) for x = 0.025 is significantly smaller than the value of coercive field observed in widely explored ceramics $Ba(Ti_{0.88}Sn_{0.12})O_3$–$0.30(Ba_{0.70}Ca_{0.30})TiO_3$ (BST-xBCT) having $d_{33} \sim 530$ pC/N [13]. The low coercive field can make the composition x = 0.025 as one of the suitable lead-free candidates for various piezoelectric applications. In addition to BST-xBCT ceramics, the value of the coercive field for x = 0.025 is also found to be significantly smaller when compared with another MPB based widely explored ceramics, *viz.,* $(K_xNa_{1-x})NbO_3$ and $(Li_xNa_{1-x})NbO_3$, which remain at the center of attraction for those working in the field of perovskite-based lead-free ferroelectric materials [281, 282]. On further increasing the Sn(x) content away from x = 0.025, the coercive field exhibit a similar trend like remnant polarization. Such a decreasing nature of the coercive field is attributed to the decrease in grain size with increasing Sn content [228].

Now, based on the above analysis, the slightly distinct behaviour of dielectric constant and ferroelectric polarization as a function of Sn(x) content can be interpreted. The remnant polarization shows a relatively higher value for x = 0.025 than x = 0 due to the aforementioned inter-ferroelectric three-phase ($P4mm + Amm2 + R3m$) coexistence region for x = 0.025, resulting in an easy polarization rotation phenomenon [38, 115]. In addition to this, peaked value in amplitudes of polar Γ_4^- phonon mode corresponding to $Amm2$ and $R3m$ phases has given a significant contribution. On the other hand, the decrease in dielectric permittivity for x = 0.025 may be attributed to the reduced fraction of 180^0

domain walls when compared with $x = 0$, which has been considered as the main extrinsic contributor in the dielectric constant of $Pb(Zr,Ti)O_3$ around morphotropic phase boundary [129]. Further, for $x = 0.05$, the dielectric constant is increased in comparison to x=0.025, but polarization is decreased. In $x = 0.025$, the three-phase coexistence is arrived due to the close proximity of T-O and O-R phase boundaries, while $x = 0.05$ consists only O-R phase boundary, leading to a two-phase coexistence. Recently in BZT-xBCT system, it has been reported that the T-O phase boundary has a smaller energy barrier than the O-R phase boundary [12]. With a similar analogy, the polarization rotation phenomenon will not be so much easier for $x = 0.05$ as it was for $x = 0.025$. Moreover, the amplitudes of Γ_4^- phonon mode for both $Amm2$ and $R3m$ phase is decreased in $x = 0.05$. These above-mentioned causes will collectively lead to decreased P_r value. However, the tetragonal ($P4mm$) phase present in $x = 0.025$ disappears completely at $x = 0.05$, and its most of the fraction has been replaced by the rhombohedral ($R3m$) phase having a significantly large amplitude of polar phonon mode, resulting in an increased dielectric constant. With further increase in Sn(x) content from $x = 0.05$ to 0.075, the two-phase ($Amm2 + R3m$) region transforms into a single $R3m$ phase having lower amplitude of Γ_4^-(R) phonon modes leading to a decrease in P_r, and dielectric permittivity. Finally, for $x = 0.10$, the P_r has exhibited minimum value because of the major cubic phase (fraction = 86.51%); however, dielectric constant is increased significantly due to the appearance of the paraelectric (cubic) to ferroelectric (rhombohedral) phase transition at room temperature.

5.3.7 Temperature-dependent Raman spectroscopic studies

In order to have further insight into the impact of Sn(x) content on tuning the various phase transitions of BCZTSnx ceramics, we have carried out the temperature-dependent Raman spectroscopic analysis for some of the compositions, *viz.,* $x = 0.025$, 0.05, and 0.075, for the temperature range 77 K-523 K. The measured temperature-dependent Raman spectra

of BCZTSnx, shows a good agreement with that of pure barium titanate as reported in previous studies [204], and hence various modes have been assigned accordingly. Fig. 5.13 shows the temperature-dependent evolution of Raman spectra of BCZTSnx ceramics corresponding to $x = 0.025$. The high temperature (398 K-523 K) phase of $x = 0.025$ has two broad peaks, corresponding to wavenumber 250 cm^{-1} and 520 cm^{-1}, which is the signature of the cubic phase [204, 227]. However, a broad hump around 725 cm^{-1}, corresponding to A_1[LO3]/E[LO3] mode can be seen which corresponds to the existence of local off-centering of the atoms, similar to one observed in all the temperature-dependent phases (rhombohedral →orthorhombic→tetragonal →cubic) of pure $BaTiO_3$ corresponding to 'B' site [107, 165, 189]. In addition, a weak peak corresponding to E[TO1] mode can also be seen, representing the local disorder of the rhombohedral type as observed in pure $BaTiO_3$ [189, 238]. On Further lowering the temperature, at 348 K, a peak appears corresponding to E[TO2]+B_1 mode, and the peak corresponding to A_1[LO3]/E[LO3] mode becomes sharp, indicating a cubic to a long-range tetragonal phase transition consistent with the dielectric studies [164, 184]. However, the signature of local rhombohedral structure can still be seen, which is due to the reason that the tetragonal phase of barium titanate is also driven by the partial ordering of the rhombohedral-like locally off-centered 'B' site cations [2]. Further, at 298 K, some more modifications occur in the Raman spectra. A new peak corresponding to A_1[TO1] mode appears which has been considered as the characteristic of the orthorhombic phase [227]. In addition, A_1[LO] mode becomes sharpen, and the peak corresponding to E[TO1] mode becomes more significant. In the studies performed in the past, it has been demonstrated that the A_1[LO] mode and E[TO1] mode appears only in the rhombohedral phase [264]. Further, the presence of sharp peaks corresponding to triple modes, *viz.,* E[TO1], A_1[LO], and A_1[TO1], represents the signature of long-range rhombohedral phase. [227, 264].

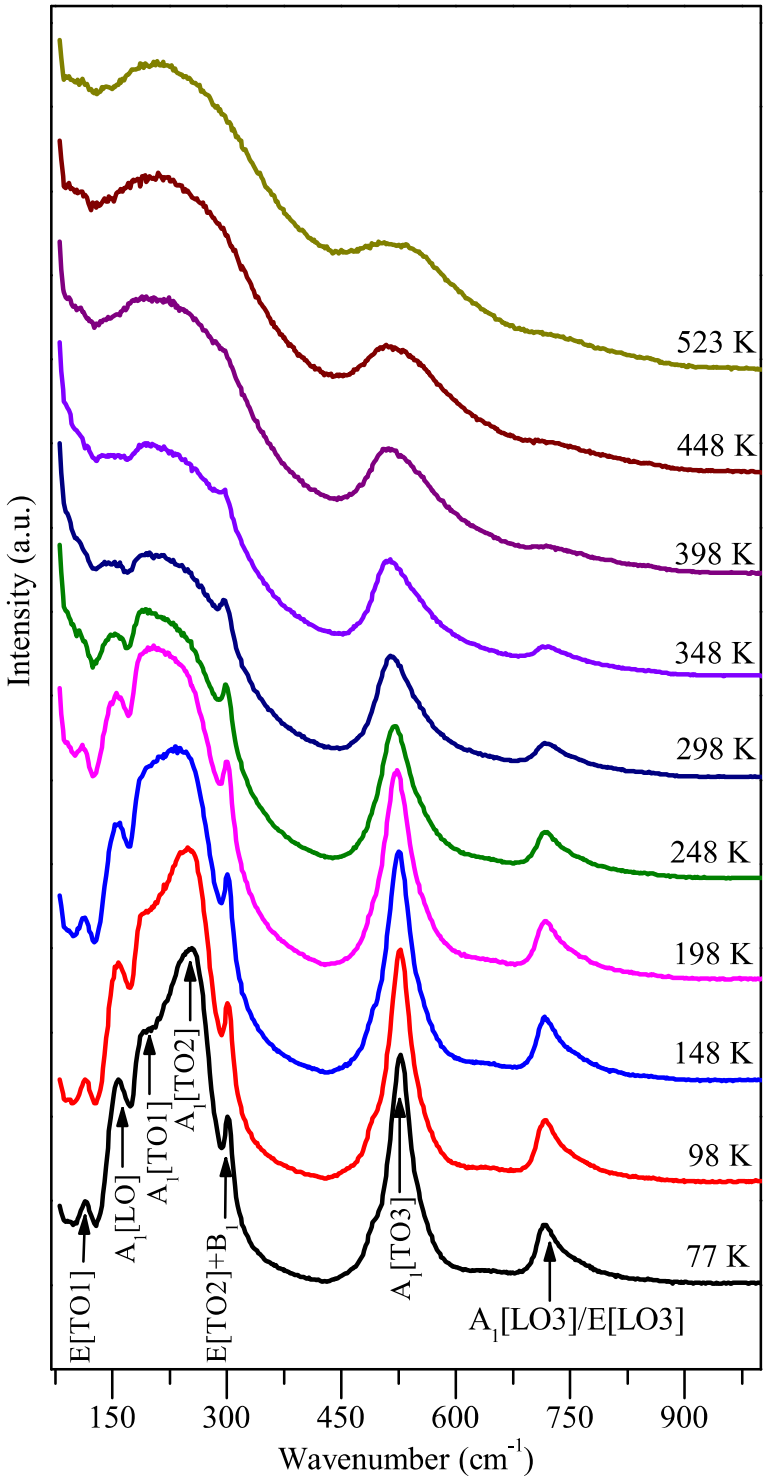

Fig. 5.13 Temperature-dependent Raman spectra of $x = 0.025$.

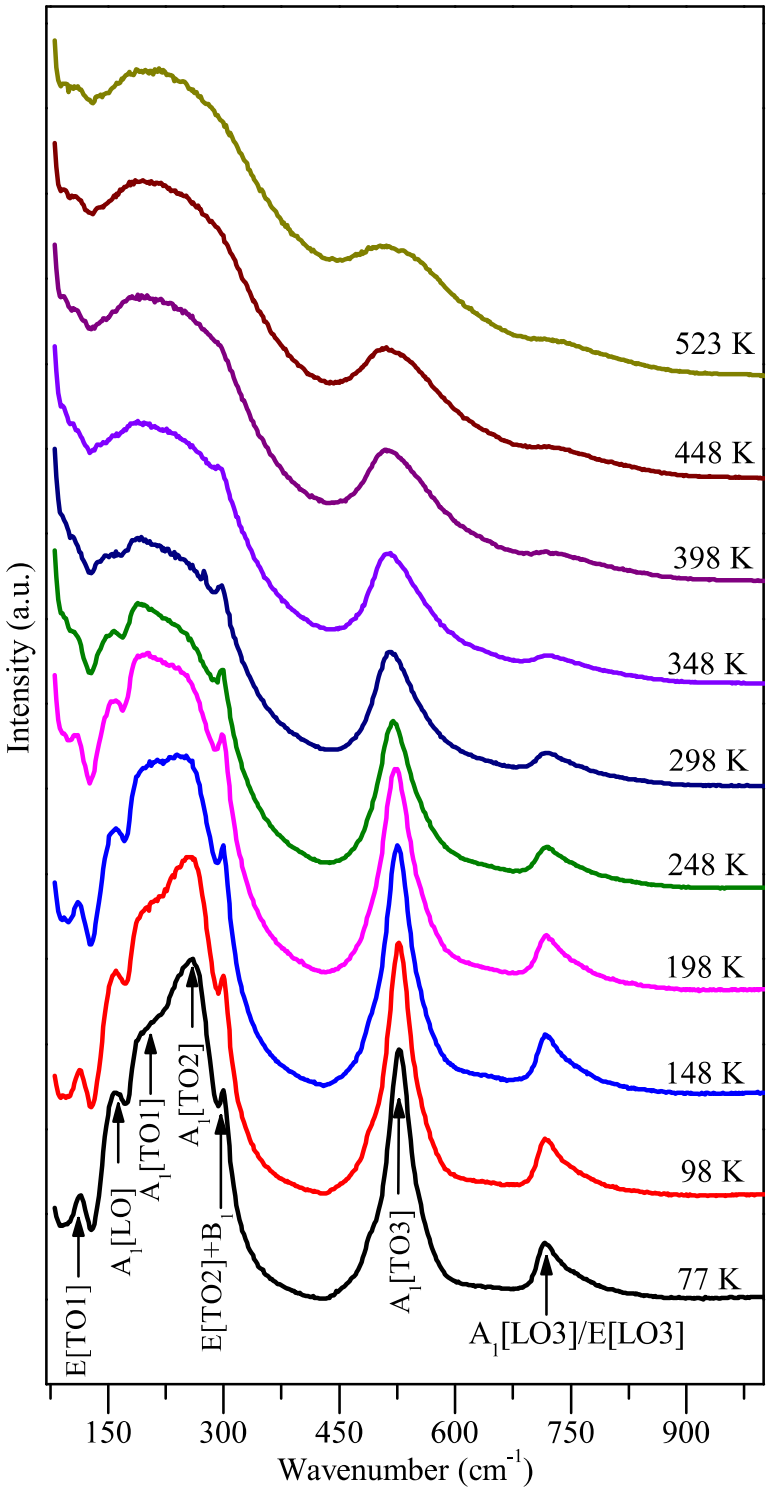

Fig. 5.14 Temperature-dependent Raman spectra of $x = 0.05$.

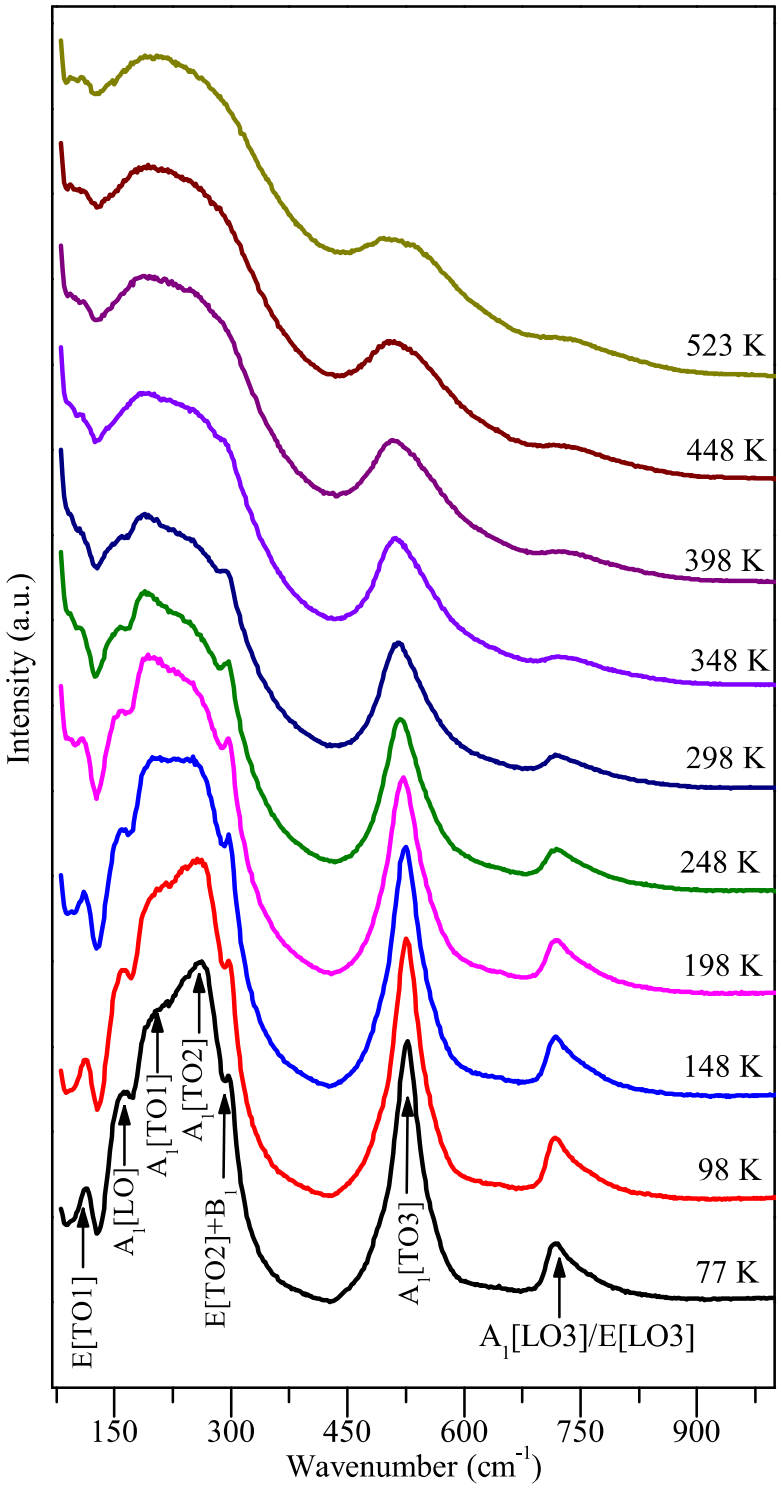

Fig. 5.15 Temperature-dependent Raman spectra of $x = 0.075$.

On the other hand, our dielectric studies have revealed the appearance of (tetragonal+orthorhombic) phase transition in the vicinity of room temperature. Thus the combined dielectric and Raman spectroscopic studies dictate a three-phase (tetragonal+orthorhombic+rhombohedral) coexistence, consistent with the X-ray diffraction studies. On further lowering the temperature, in addition to A_1[LO], and A_1[TO1] modes, the peak corresponding to the E[TO1] mode sharpens, dictating a rhombohedral phase [189], for 248 K. Furthermore, all the modes present at 248 K, persist till 77 K, revealing the presence of a rhombohedral structure down to the lowest measured temperature.

Further, like $x = 0.025$, the composition $x = 0.05$ also exhibits the Raman spectra above the Curie-temperature, *i.e,* in the paraelectric cubic ($Pm\bar{3}m$) region (see Fig. 5.14), predicting the presence of atomic disorder at short-range scale [189]. The similar features have also been detected in the Raman spectra of $BaTiO_3$ above the Curie temperature [204]. When the temperature is decreased, at 348 K, the Raman spectra resembles the features of pure $BaTiO_3$ observed at ambient conditions. On further lowering the temperature, at 298 K, an additional peak corresponding to A_1[LO] mode appears along with the presence of E[TO1], A_1[TO1] modes which corresponds to the rhombohedral-like structure [189]. However, the possibility of the two-phase (orthorhombic+rhombohedral) coexistence can not be excluded since the dielectric study demonstrates that the orthorhombic to rhombohedral phase transition lies in the vicinity of room temperature, and also some corresponding peaks observed in Raman spectra are broadened in nature. Thus the Raman spectra around 298 K resembles two-phase (orthorhombic+rhombohedral) coexistence as confirmed via X-ray diffraction studies. On further lowering of temperature, the triple mode (E[TO1], A_1[LO], and A_1[TO1]) characteristic of the rhombohedral phase become more prominent, suggesting a rhombohedral phase of $BaTiO_3$ till the lowest measured temperature.

In the case of $x = 0.075$, the measured Raman spectra at low temperatures show similar peaks as the one observed for $x = 0.025$ and $x = 0.05$, which confirms a low-temperature rhombohedral phase for $x = 0.075$ (see Fig. 5.15), All the modes consistent with the rhombohedral phase persist till 298 K leading to a rhombohedral phase in the vicinity of room temperature in line with the dielectric studies. Further, at temperatures higher than 298 K, two broad peaks can be seen around wavenumber 250 cm^{-1} and 515 cm^{-1}, which corresponds to the cubic phase. However, the peak present around 725 cm^{-1} still survives, although with a significantly broadened nature, indicating some local off-centered displacement of the atoms present in the cubic matrix, as mentioned for $x = 0.025$ and 0.05. Thus the analysis of the temperature-dependent Raman spectroscopic data reveals that the increase in Sn(x) content is stabilizing the low-temperature rhombohedral phase at room temperature, which is in well agreement with the conclusions made by X-ray diffraction and temperature-dependent dielectric studies.

5.4 Conclusion

The present work demonstrates a detailed analysis of the Sn(x) induced crystallographic phase evolution and its correlation with the physical properties of a scientific and technologically important eco-friendly BCZTSnx ceramics. The X-ray diffraction analysis has revealed the presence of several phase coexistence regions, with the stabilization of low symmetry rhombohedral ($R3m$) phase at room temperature, as a function of Sn(x) content, in line with the combined dielectric and Raman spectroscopic studies. Further, the composition $x = 0.025$, having an inter-ferroelectric three-phase ($P4mm + Amm2 + R3m$) coexistence, exhibits a high ferroelectric polarization and low coercive field. The high polarization of $x = 0.025$ is attributed to the peaking behaviour in amplitudes of ferroelectric Γ_4^-(O) and Γ_4^-(R) phonon modes and the easy polarization rotation phenomenon [38, 115]. The easy polarization rotation phenomenon, as previously observed in various

multi-phase systems [204, 283], and decrease in grain size has been considered as a cause of low coercive field. Thus we find that the fabrication of a smart system with enhanced macroscopic polarization is inherent in the high amplitudes of the ferroelectric phonon modes (Γ_4^-) at the microscopic level. Moreover, owing to its fascinating ferroelectric properties, the composition $x = 0.025$ may be a promising candidate for various technological applications.

In the next chapter, we have extended our studies for higher Sn content and explored the possibility of relaxor ferroelectric nature due to the presence of distinct cations corresponding to the 'B' site of the perovskite structure having a significant difference in their ionic radii.